DOE/ER/01198--T43

ALUMINUM NITRIDE - SILICON CARBIDE WHISKER COMPOSITES: PROCESSING, PROPERTIES, AND MICROSTRUCTURAL STABILITY

DOE/ER/01198--T43

DE91 001907

BY

MICHAEL THOMAS CROSS

B.S., University of Washington, 1987

THESIS

Submitted in partial fulfillment of the requirements
for the degree of Master of Science in Ceramic Engineering
in the Graduate College of the
University of Illinois at Urbana-Champaign, 1990

Urbana, Illinois

ABSTRACT

Aluminum nitride - silicon carbide whisker composites with up to 20 vol% whiskers were fabricated by pressureless sintering (1750°-1800°C) and by hot-pressing (1700°-1800°C). Silicon carbide whiskers were found to degrade depending on the type of protective powder bed used during sintering. Whiskers were found to degraded in high oxygen containing samples by reaction with sintering additives. Whisker degradation was also due to the formation of silicon carbide - aluminum nitride solid solution. No whisker degradation was observed in hot-pressed samples. For these samples Young's modulus and fracture toughness were measured.

A 33% increase in the fracture toughness was measured by the indentation technique for a 20 vol% whisker composite. Operative toughening mechanisms were investigated using scanning electron microscopy. Crack deflection and whisker bridging were the dominant mechanisms. It was also shown that load transfer from matrix to whiskers can be a contributing factor to toughening.

DEDICATION

To my wife Suzanne, for her patience and support.

He who finds a wife finds what is good
and receives favor from the Lord.
Proverbs 18:22

To my parents, for their encouragement
through the years.

ACKNOWLEDGEMENTS

To Dr. A. Zangvil for his insight, direction, and encouragement during the course of this research.

To Dr. Y. Xu for his gracious assistance and for many fruitful discussions.

To C. C. Lin and Y. Kim for their help and friendship.

To J. Rhodes and B. Rodgers at Advanced Composite Materials Corporation for their assistance.

To the staff of the Center for Microanalysis of Materials for their assistance: Dr. N. Kaufherr and Dr. J. B. Woodhouse.

The author wishes to acknowledge research support by the U. S. Department of Energy, Division of Materials Sciences, under Contract DE-AC02-76ERO1198.

TABLE OF CONTENTS

LIST OF TABLES

LIST OF FIGURES

I. INTRODUCTION

Aluminum nitride (AlN) is currently being developed for use as an advanced electronic substrate material because of its high thermal conductivity, high electrical resistivity, and its close thermal expansion match to silicon. Aluminum nitride also has potential for use as a structural ceramic because of its oxidation resistance, high elastic modulus, and strength. But like many other ceramics, it has a low fracture toughness, on the order of 2.6-3.0 $MPa \cdot m^{1/2}$ [1-3].

The purpose of this study is to investigate the potential of toughening AlN ceramics by reinforcing them with silicon carbide (SiC) whiskers. The rationale for using SiC whiskers as the reinforcing phase is twofold. First, SiC whiskers have improved the strength, fracture toughness, and creep resistance of many ceramics such as aluminum oxide (Al_2O_3) [4-13], mullite [4, 10, 14, 15], and silicon nitride (Si_3N_4) [10, 16-21]. Many of these composites have fracture toughnesses greater than 8 $MPa \cdot m^{1/2}$, compared to toughnesses of ≈ 3-6 for the unreinforced material. Secondly, extensive solid solution exists in the SiC-AlN system which may be used to tailor the AlN-SiC whisker interface. This is significant since the properties of ceramic composites are known to be dominated by the interface.

Published reports of AlN-SiC whisker composites are very limited. Yamada reported an increase in the effective fracture energy at high temperature due to whisker pullout, but did not mention microstructure, interfaces, or fracture toughness values [10]. In the present study we seek to understand the effects of process conditions on composite microstructure, interfaces, and operative toughening mechanisms in addition to evaluating the toughening potential.

II. LITERATURE REVIEW

A. Aluminum Nitride

A review of the current literature shows AlN to be of interest mainly due to its potentially high thermal conductivity, which can be greatly influenced depending upon the method of fabrication used. As a structural ceramic, the physical properties of AlN are attractive; however, its fracture toughness is low. The fracture toughness of ceramics can be increased by the composite approach, e.g., reinforcement with whiskers. A review of the SiC-AlN system is given below in order to assess the feasibility of an AlN-SiC whisker composite and the potential for interface modification.

1. Thermal Conductivity

Hot-pressed AlN without additives has a thermal conductivity far below that for pure AlN single crystals. The low thermal conductivity of AlN without additives has been attributed to impurities. The effect of impurities on thermal conductivity has been studied by Slack with particular attention to oxygen impurity [22]. Slack proposed that the incorporation of oxygen in AlN occurs by dissolution of Al_2O_3 by the following reaction:

$$Al_2O_3 \rightarrow 2Al_{Al} + 3O_N + V_{Al} \qquad \{1\}$$

where V_{Al} denotes a vacancy on an aluminum site. These aluminum vacancies scatter phonons which effectively lower the thermal conductivity. Improved thermal conductivity in sintered samples can be achieved by reducing the oxygen content of AlN powders [23].

The most recent work on achieving high thermal conductivity of AlN ceramics has concentrated on removing dissolved oxygen from the AlN lattice by the addition of sintering aids. Oxygen (Al_2O_3) is removed

from AlN grains by reaction with the sintering aid to form various aluminate minor phase(s). Rare-earth oxides and alkaline-earth oxides have been used to produce AlN ceramics with increased thermal conductivity. Most of this work has concentrated on the use of Y_2O_3 and CaO additions. Cathodoluminesence has shown that the addition of Y_2O_3 effectively lowers the oxygen content within AlN grains [24]. Table 1 lists the thermal conductivity of several AlN ceramics.

Table 1. Thermal Conductivity of AlN Ceramics.

Composition	Thermal Conductivity (W/m·K)	References
AlN, single crystal	320	25
HP AlN	50	26
HP, AlN	85	27
HP, AlN + 2 wt% CaO	135	27
HP, AlN + 2 wt% CaC_2	180	27
HP, AlN + 2 wt% Y_2O_3	145	27
PL, AlN + Y_2O_3	>150	28,29,30
PL, AlN + 2 wt% Y_2O_3 (2.3-1.1 wt% O_2)	70-151	31
PL, AlN + 4 wt% Y_2O_3 (2.3-1.1 wt% O_2)	107-193	31
PL, AlN + 2.1 wt% $3CaO{\cdot}Al_2O_3$	175	32

HP = Hot-pressed
PL = Pressureless sintered

2. Fabrication

Aluminum nitride ceramics can be fabricated by conventional techniques such as hot-pressing and pressureless sintering. Generally, AlN can be hot-pressed to full density because the oxygen impurity of the AlN powder aids in densification [33]. However, the oxygen impurity alone is not enough for pressureless sintering AlN to full density. In this case, sintering aids are used. Many different sintering aids have been used to fabricate AlN ceramics with most of the

attention being directed toward the use of alkaline earth oxides and the rare-earth oxides, particularly Y_2O_3. Table 2 lists various compositions of AlN ceramics that have resulted in high density.

Table 2. Various Compositions of High Density AlN Ceramics.

Composition	Density (g/cm^3)	References
No Additives		
HP, AlN (< 2 wt% O_2) up to 2000°C	Low	33
HP, AlN (> 3 wt% O_2) 1800°C	Full	33
PL, AlN, 1800°-2000°C	Poor	26
PL, AlN	85% Theo.	34
PL, AlN (1 wt% O_2), tape casting, 1850°C	98.7% Theo.	32
Alkaline Earth Oxides		
PL, AlN + 1 mol% CaO (or SrO), 1800°-1900°C	Full	26
PL, AlN + 1 mol% CaO, 1700°C	Full	35
PL, AlN + 1 mol% LiO_2, 1800°C	Full	35
PL, AlN + 2.1 wt% $3CaO{\cdot}Al_2O_3$, 1800°C	Full	32
PL, AlN+CaO+Y_2O_3+La_2O_3+CeO_2+SiO_2, 1600°C	Full	36
Rare-Earth Oxides		
PL, AlN + 1-4 wt% Eu_2O_3, 1800°C	97-98%	37
PL, AlN + lanthanide oxides, 1850°C	Full	31
PL, AlN + 3 wt% lanthanide oxides, 1800°C	Full	38
PL, AlN + 2-12 wt% Y_2O_3, 1850°C	96-99.5%	31
PL, AlN + 0.5 wt% Y_2O_3, 1800°-1850°C	Full	38

HP = hot-pressed
PL = pressureless sintered

These sintering aids react with Al_2O_3 on the AlN powder surface to form intergranular liquid phase(s) during sintering. The postulated sintering mechanism of AlN with Y_2O_3 is the formation of a liquid phase above 1760°C as found in the Y_2O_3-Al_2O_3 system [39]. X-ray diffraction (XRD) shows that Y_2O_3 additions form $Y_3Al_5O_{12}$ (yttrium

aluminum garnet = YAG) as the main aluminate phase with $Y_4Al_2O_9$ present with increasing Y_2O_3 addition [27, 31, 38].

Another phase that is observed in AlN ceramics is a γ-aluminum oxynitride (γ-AlON) phase. γ-AlON is an intermediate compound between AlN and Al_2O_3, of the approximate composition $Al_{23}O_{27}N_5$, that forms above 1700°C [40]. The presence of both YAG and AlON in sintered AlN has been reported [41].

Sintering of AlN is typically done in a nitrogen atmosphere to suppress decomposition. The use of AlN powder as an embedding medium to create a self-stabilizing atmosphere during sintering is also commonly used [3, 31, 35-37, 42].

3. Properties

Aluminum nitride is a covalent compound with a hexagonal crystal structure of the wurtzite type (space group P63mc). The cell parameters (a = 3.111 Å; c = 4.979 Å) vary slightly with oxygen content. Its theoretical density is 3.26 g/cm^3 [43], and its average thermal expansion coefficient (100°-1000°C) is 5.7 x 10^{-6}/°C [44]. Aluminum nitride is reported to decompose congruently to the elemental gases in the temperature range of 1580°-1707°C [45].

In air or oxygen, AlN sintered without additives generally begins to oxidize towards 800°C [45], with oxidation becoming significant at 1100°C [46]. From 1200°C-1450°C the oxidation kinetics are parabolic as a compact scale of Al_2O_3 is formed which adheres well to the substrate. Above 1500°C kinetics become linear while the oxide coating is no longer protective due to Al_2O_3 grain growth [45].

Aluminum nitride sintered with oxide additions has an oxidation behavior in air which is about the same as that of AlN without

additives. However, oxidation resistance is normally lowered at higher temperatures because of early crystallization of the aluminate phases, which results in microcracking of the protective scale [45].

The mechanical properties of hot-pressed and sintered AlN have been reported. Young's modulus, strength, and fracture toughness of AlN ceramics are listed in Table 3.

Table 3. Mechanical Properties of AlN Ceramics.

Composition and Conditions	Value	Reference
Young's Modulus	**GPa**	
HP, AlN (parallel to HP direction)	324	2
HP, AlN (perpendicular to HP direction)	342	2
HP, AlN	322	47
HP, AlN	314	1
PL, AlN + 3 wt% Y_2O_3 (>98.5% dense)	308	48
Strength	**MPa**	
HP, AlN	377	3
HP, AlN	310	2
HP, AlN	255	49
HP, AlN + Y_2O_3 +SiO_2 (fibrous grains)	400-690	50
PL, AlN + 2 wt% CaO (fine gr./coarse gr.)	313/270	3
PL, AlN + CaO (or Y_2O_3) - at 1300°C for 48 hr.	200	45
Fracture Toughness	**MPa·m$^{1/2}$**	
HP, AlN (3 pt. bend)	2.6	1
HP, AlN (3 pt. bend)	2.7	2
HP, AlN (biaxial testing of disks)	3.6	3
HP, AlN (indentation,98 N)	1.8	3
PL, AlN + 2 wt% CaO (biaxial testing) fine gr.	2.9	3
PL, AlN + 2 wt% CaO (biaxial testing) coarse gr.	3.1	3
PL, AlN + 2 wt% CaO (indentation,98 N) fine gr.	1.5	3
PL, AlN + 2 wt% CaO (indentation,98 N) coarse gr.	1.8	3

HP = Hot-pressed
PL = Pressureless sintered

B. Silicon Carbide - Aluminum Nitride System

For any potential composite, knowledge of individual phase stability (thermally, chemically, etc.) as well as interface stability is needed. This knowledge can be used to avoid detrimental reactions or cause beneficial reactions which modify the interface; therefore, the literature concerning the SiC-AlN system is reviewed below.

Silicon carbide is a high temperature structural ceramic that has also attracted interest for its electrical properties. In the past decade there has been increasing interest in possibilities for alloying of SiC with other ceramic compounds in order to modify and control various mechanical and physical properties and to improve sinterability. A number of compounds such as boron carbide (B_4C), Al_2O_3, boron nitride (BN), and beryllium oxide (BeO) have been added in small amounts as sintering aids, while other compounds such as AlN and aluminum oxycarbide (Al_2OC) can be added in large amounts to form extensive solid solutions with SiC and modify its properties. Zangvil and Ruh [51] recently reviewed those additives to SiC that can potentially modify properties (other than sinterability) by the formation of solid solutions, control of microstructure development, formation of compounds, and control of polytype stability.

Silicon carbide is a covalent compound which can exist in the cubic or hexagonal crystal structures. Silicon and carbon are in tetrahedral coordination, and crystal structures are comprised of layers of these tetrahedra. The stacking sequence of tetrahedra determines the symmetry [52]. The structure can be described using Ramsdell notation where the number is the number of close-packed Si-C double layers and the letter denotes the crystal symmetry. The 3C

polytype is cubic and designated β-SiC, whereas hexagonal or rhombohedral forms (2H, 4H, 6H, 15R, 21R) are designated α-SiC. Aluminum nitride is also a covalent compound which has the hexagonal 2H (wurtzite) structure and lattice parameters very close to those of SiC. Table 4 lists the lattice parameters of SiC and AlN, as well as their elastic moduli (E) and thermal expansion coefficients (α).

Table 4. Lattice Parameters and Physical Properties of SiC and AlN.

Material	Space Group	Lattice Parameter a (Å)	c (Å)	E (GPa)	α (10^{-6}/°C) (20-1000°C)
SiC	Fd3m(cubic)	4.398		-	4.45 [53]
SiC	P63mc (2H)	3.076	5.048	410 (α-SiC) [54]	3.63 [53]
AlN	P63mc (2H)	3.111	4.979	322 [47]	5.7 [44]

Aluminum nitride has been shown to stabilize a number of SiC polytypes. A tentative phase diagram for the SiC-AlN system as presented by Zangvil and Ruh [55] is shown in Figure 1. In this work phase relationships were determined by x-ray diffraction (XRD) and analytical electron microscopy of local equilibria among adjacent phases in hot-pressed samples and in diffusion couples. A wurtzite-type 2H (δ) solid solution was found to extend from an impurity-sensitive lower limit of 17 to 24 mol% AlN up to 100 mol% AlN. Solid solutions were shown to have the general formula $(SiC)_{1-x}(AlN)_x$ and belong to the SiC-AlN pseudobinary system. Mechanical properties of some SiC-AlN solid solutions (SS) and two-phase composites have been reported and are listed in Table 5. The elastic modulus was found to decrease with increasing AlN content, and to be greater in solid solutions compared to the equivalent two-phase compositions [47].

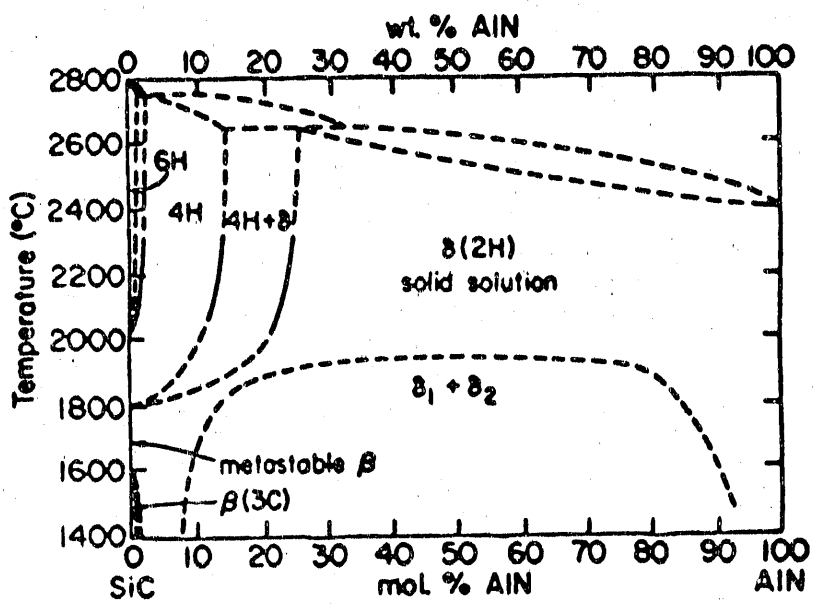

Figure 1. Tentative Phase Diagram of the SiC-AlN System. [55]

Table 5. Mechanical Properties of SiC-AlN Solid Solutions and Two-Phase Composites.

Solid Solutions (SS) / Composites		E (GPa)	Reference
SiC + 10.2 % AlN	/ SiC + 10% AlN	407 / 396	47
SiC + 36.9% AlN	/ SiC + 37.5% AlN	391 / 371	47
SiC + 49.4% AlN	/ SiC + 50% AlN	365 / 349	47
SiC + 79.8% AlN	/ SiC + 75% AlN	350 / 338	47
		K_{IC} (MPa·m$^{1/2}$)	
SiC		4.5	56
SiC + 20% AlN (SS)		3	56

Analytical electron microscopy shows that defect-free or nearly free β-SiC cannot dissolve more than 1% or 2% AlN. Lattice parameter data also supports this finding [56]. Some β-SiC with up to 4% AlN was found in samples hot-pressed at 1850°-2100°C, but this was always heavily faulted β-SiC; i.e., it included a large proportion of hexagonal-type sites, which seems to be a condition for extensive AlN solubility in SiC [55].

The transformations from β and from various α polytypes into 2H solid solutions occur by diffusion-controlled transformations through a layer-displacement mechanism with transformation zones up to 30 nm wide [55]. The β-phase would either first transform into α and then into the 2H solid solution, or would remain as β, but develop faults in the cubic structure and gradually incorporate AlN. This transformation is delayed at low temperature (< 2100°C), and thus very low apparent diffusion rates of AlN into SiC are measured [57]. Difficulty in measuring the diffusion of AlN into SiC was also due to the formation of a series of polytypes with compositional "steps". In general, the diffusion depth, and therefore the diffusion coefficient, of AlN in SiC were considerably lower, by an estimated one order of magnitude, than those of SiC in AlN. This is in agreement with the fact that SiC is more strongly bonded than AlN.

Estimates of SiC diffusion into AlN were made in diffusion couples in the high temperature range (2100°-2300°C) and in hot-pressed samples in the low temperature range (1850°-1950°C) [57]. Scanning transmission electron microscopy (STEM) and energy-dispersive x-ray spectroscopy (EDS) of silicon and aluminum, with an estimated analytical lateral resolution of less than 100 nm, was used

to measure the diffusion distance of SiC into AlN. Figure 2 shows these results as a function of temperature. Extrapolating these results over the temperature range used in the present study (1700°-1800°C), the expected diffusion distance of SiC into AlN is ≤ 0.2 μm.

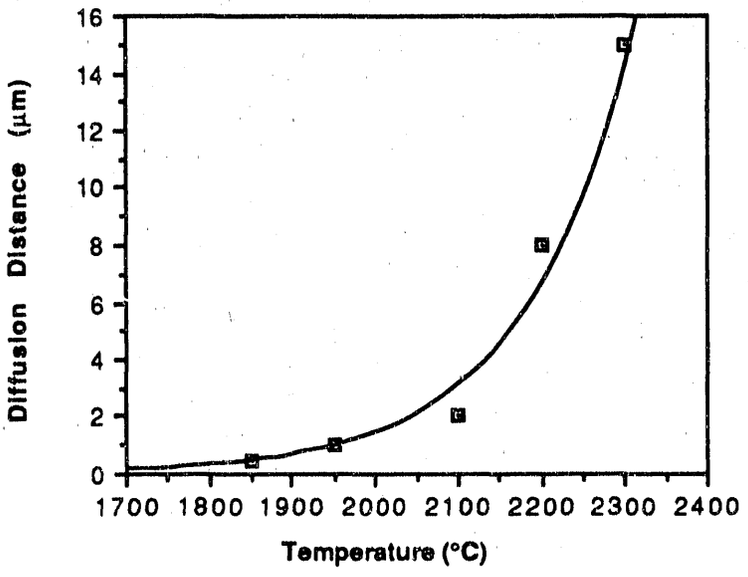

Figure 2. Approximate Diffusion Distance of SiC into AlN, based on data from [57].

The presence of a miscibility gap within the SiC-AlN system was proposed by Ranfaniello *et al.* [56] and is shown in Figure 1. It exists below ≈ 1900°C from between 10 mol% AlN and 90 mol% AlN. This is also the operating temperature and composition range of the present study and may be relevant to microstructural development.

C. Ceramic Whisker Composites

Reinforcing ceramics with other ceramic phases is the basis of a class of composite materials known as ceramic matrix composites (CMC's). A variety of reinforcements can be used such as particles, fibers, and whiskers. Whisker reinforcement, particularly SiC whiskers, has gained popularity in recent years. Silicon carbide whiskers have significant potential as reinforcements for ceramic matrix composites because of their strength, high elastic modulus, and stability at elevated temperatures. Silicon carbide whiskers can be made by a vapor-liquid-solid (VLS) process [58] or a more economical process involving the pyrolysis of silica and carbon from ground rice hulls [59]. VLS processed SiC whiskers are typically 5 to 6 μm in diameter and up to 100 mm in length, whereas whiskers produced from rice hulls are typically submicron in diameter and range from 10 to 80 μm in length. VLS-processed whiskers are not currently as widely used as whiskers derived from rice hulls because of limited availability and the presence of catalyst balls from the VLS process which can result in large defects in the composites.

Nutt [60] recently studied the defects in SiC whiskers produced from rice hulls. These whiskers are a faulted 3C (β-phase) with the whisker growth axis along the [111] direction. A high density of planar faults, such as stacking faults and narrow twins, were found to lie on close-packed planes perpendicular to the whisker axis. The faulting results in regions of complex mixtures of α and β polytypes arranged in thin lamellae normal to the whisker axis. These defects are manifest as fine dark lines that resemble lattice fringes. Small cavities, generally 5 to 10 nm in size, are often observed; they are usually

confined to the core region of the whisker. Calcium inclusions are also often observed in that region.

The mechanical properties of SiC whiskers have been reported. The high elastic modulus (E) and high strength of SiC whiskers are listed in Table 6.

Table 6. Mechanical Properties of Silicon Carbide Whiskers.

Make	Dimensions (μm) Diameter, length	Mechanical Properties E (GPa)	Strength (GPa)	Reference
VLS	≈ 5 μm, 5mm	581	7-32, 8.4 avg.	61
SC-9 Arco	0.6, 10-80	689	6.89	62
Tateho	0.6, 10-80	482	20	62
VC-1, Versar	1-10, 20-400	551	18	62

D. Indentation Fracture Toughness

A popular experimental technique for measuring or estimating the fracture toughness (K_{IC}) of ceramic materials is the indentation method. This involves the loading and unloading of a Vickers diamond point indenter onto the polished surface of the test sample and the subsequent measurement of the crack lengths extending from the four corners of the residual diamond indentation. Figure 3 is a schematic of the indentation process and the residual crack pattern. The attraction of this technique is the ability to test samples of small size and its relative simplicity.

Calculation of the fracture toughness by Vickers indentation is based on two premises [63, 64]:

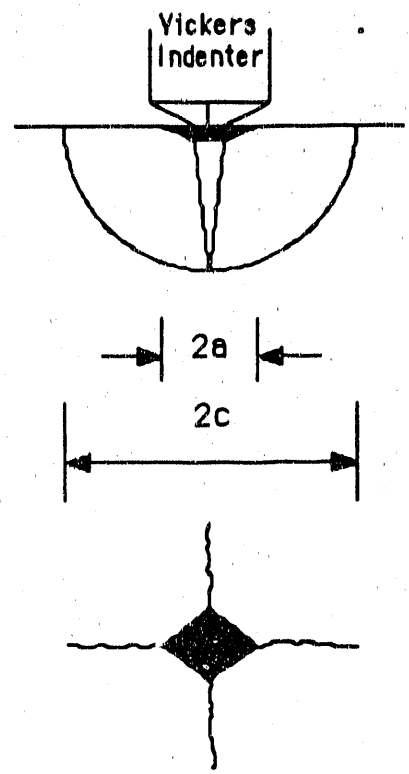

Figure 3. Schematic of Vickers Indentation with Half-Penny Shaped Cracks of Length 2c.

(1) The cracks are well-developed, half-penny in shape.

(2) Half-penny cracks are centrally loaded with a crack-opening point force.

The first requirement above is satisfied at the lower limit by the minimum requirement $c \geq 2a$ and the upper limit by material chipping or limitation of material thickness. The second premise requires a properly aligned indenter and parallel sample surfaces with the indenter being perpendicular to the sample surface. Also implicit in the indentation fracture toughness equations is indentation of a homogeneous isotropic material.

When the above two requirements are satisfied, the radius of a half-penny crack (c) is related to the indentation load (P) by

$$c = kP^{2/3} \quad (2)$$

The driving force for crack growth is characterized by a residual stress intensity factor of the form [65]:

$$K_r = \chi_r P/c^{3/2} \quad (3)$$

where χ_r is a constant. Based on this, Lawn and Fuller [65] presented the following equation for calculating K_{IC} assuming penny-shaped cracks:

$$K_{IC} = [1/(\pi^{3/2} \tan \psi)]P/c^{3/2} \quad (4)$$

where ψ is the half-angle of the Vickers indenter, equal to 68°. It is noted that the fracture toughness equation contains no materials parameters.

Lawn *et al.* [66] investigated the importance of the residual stress field around a sharp indenter. The residual stress field consisted of two superposable components to the net driving force of the crack system: an elastic (reversible) and a residual (irreversible) component. At the indentation surface the elastic component is compressive and the residual component tensile. Thus, the radial cracks grow to their final lengths as the indenter is unloaded. Considering this and a residual stress intensity of the form determined by Lawn and Fuller [65], the following equation for K_{IC} was proposed:

$$K_{IC} = \chi_r P/c_o^{3/2} = \zeta(E/H)^{1/2}P/c_o^{3/2} \quad (5)$$

where E is the elastic modulus and H is the hardness. Anstis *et al.* [67] determined the material-independent dimensionless constant (ζ) to equal 0.016 ± 0.004 from curve fitting data for a number of ceramic materials.

The need for a simple method for determining the elastic modulus-to-hardness ratio (E/H) prompted Marshall *et al.* [68] to develop a method using Knoop indentation. This method is based on the measurement of elastic recovery of the in-surface dimensions of Knoop indentations. When fully loaded, the ratio of the diagonal dimensions (a and b) of the Knoop contact area is defined by the indenter geometry (a/b = 7.11). On unloading, elastic recovery reduces the shorter diagonal length (a), but leaves the longer diagonal (b) relatively unaffected. The extent of recovery depends on the hardness-to-modulus ratio, a measure of which is given by the distortion of the residual impression characterized by the ratio b'/a'. The ratio b'/a' is related to the indentation by

$$b'/a' = b/a - \alpha H/E \qquad \{6\}$$

where $\alpha = 0.45$ was obtained by fitting experimental data from various ceramics. The ratio H/E is then given as

$$H/E = (0.141 - b'/a')/0.45 \qquad \{7\}$$

where a' and b' are the measured dimensions of the residual Knoop impression. The estimated error in determining H/E is < 10% when H/E ≥ 0.03.

As mentioned, implicit in the indentation fracture toughness equations is the indentation of homogeneous, isotropic materials. It is not clear if these equations can be strictly applied to a composite material, especially to a whisker composite where there tends to be preferential orientation of the whisker during processing. Recently indentation fracture toughness measurements were made on hot-pressed Al_2O_3-SiC whisker composites [69]. Values of the fracture toughness were found to vary greatly depending on the orientation of

the indented plane relative to the hot-pressed direction because of preferred whisker orientation. Nevertheless, it is common to use the aforementioned indentation techniques for composites, and in the present work we will assume that this is valid in a CMC with homogeneously distributed particles or whiskers, provided that crack lengths are much longer than the interparticle separation.

E. Toughening Mechanisms

The toughening of ceramics by whiskers generally includes contributions from crack deflection, debonding, crack bridging, and pullout [70, 71]. Each of these contributions places different requirements upon the microstructure. While the contribution from crack deflections is only governed by reinforcement shape and volume fraction [72], the other contributions depend on the mechanical properties of the interface, the whisker strength/toughness, and the whisker radius, as well as volume fraction [73].

1. Crack Deflection

The following discussion on crack deflection toughening was proposed by Faber and Evans [72]. Second phase particles near a crack tip cause a reduction in the stress intensity by perturbing the propagating crack front. Two dominant perturbations exist; crack bowing, which produces a non-linear crack front, and crack deflection, which produces a non-planar crack. Crack deflection is assumed to be the dominant perturbation.

Toughening by crack deflection arises when the crack front interacts with the microstructure, producing a non-planar crack that is subject to a reduced stress intensity. Crack deflection can occur due

to the presence of residual strains or from the existence of weakened interfaces. Residual strains result from elastic modulus and/or thermal expansion (α) mismatch between the matrix and reinforcing particles. If the particles have a smaller α, hoop tension and radial compression exist in the matrix and the particle is under compression. This is the expected situation in AlN-SiC whisker composites since $\alpha_{SiC} < \alpha_{AlN}$ ($\alpha_{SiC} = 4.5 \times 10^{-6}/°C$, $\alpha_{AlN} = 5.7 \times 10^{-6}/°C$). In this case, the crack is attracted to the particle and interfacial compressive stresses arise which increase the effective shear resistance of the interface. If the particles have a larger α, hoop compression and radial tension exist in the matrix and the particle is under tension. In this case, the crack is deflected around the particle. The direction of crack deflection appears, however, to have little effect on the magnitude of the toughening [72].

When a crack approaches a second phase particle it will characteristically tilt out of its original plane. Subsequent advance of the crack may result in crack front twist. Tilted and twisted cracks are subject locally to mixed mode loading; the tilted crack has Mode I (opening) and Mode II (sliding) contributions to the stress intensity while the twisted crack has Mode I and Mode III (tearing). The increase in fracture toughness imparted by deflection of the crack is determined from the local stress intensities at the tilted and twisted portions of the crack front.

Toughness increase due to crack deflection was found to be independent of particle size, but dependent on second phase shape and volume fraction. Rod shaped particles of high aspect ratio (length to diameter) were shown to be more effective in toughening than

spherical or disk-shaped particles. A maximum fourfold increase in fracture toughness was predicted with the majority of this increase due to crack twist rather than tilt. Toughening was predicted to increase with volume fraction of the second phase, asymptotically approaching a maximum at 20 vol%. Reduced toughness would occur at higher concentrations due to particle overlap.

The crack deflection model was confirmed experimentally in a barium-silicate glass ceramic containing a spherical crystalline phase, and in hot-pressed Si_3N_4 [74]. Increased toughness in the glass ceramic with spherical particles was consistent with predictions. The aspect ratio of Si_3N_4 grains was varied by changing the relative amounts of α-Si_3N_4 and β-Si_3N_4 in the starting powder. Toughness and deflection angles monotonically increased with aspect ratio, in agreement with theory. The crack deflection mechanism has been observed in hot-pressed SiC-Al_2O_3 and SiC-ZrO_2, where crack deflection along grain boundaries (weak interfaces) showed a notable increase in toughness compared to sintered α-SiC which fractured transgranularly [75].

2. Crack Bridging

Toughening by bridging is induced by debonding along the fiber (whisker)/matrix interface [70]. The debonding allows the whiskers to remain intact within a small bridging zone behind the crack [70], as shown in Figure 4. The magnitude of the toughening depends on the extent of debonding, the mode of reinforcement failure, and residual stress effects [70, 77].

Initial debonding along the interface requires the ratio of the interface to whisker fracture energies Γ_i/Γ_f to be small enough to lie

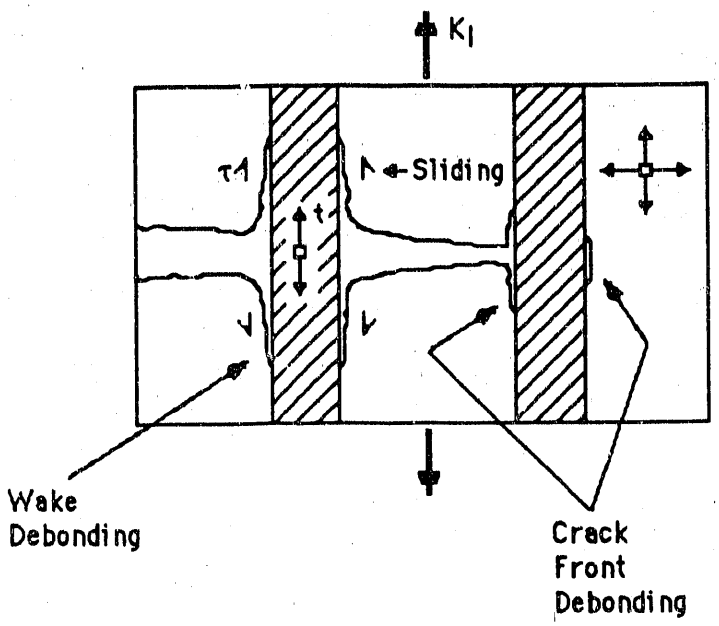

Figure 4. Schematic of a bridging zone in a reinforced composite [76].

within the debond zone at the proper whisker orientation, as defined in Figure 5 [76]. When there is no elastic mismatch between the whisker and matrix, and $\phi = 90°$, debonding occurs when Γ_i/Γ_f is less than ≈ 0.25. As ϕ decreases, debonding occurs at higher Γ_i/Γ_f ratios. Debonding tends to occur at higher Γ_i/Γ_f ratios when there is positive elastic mismatch, and at slightly lower Γ_i/Γ_f ratios when there is negative elastic mismatch.

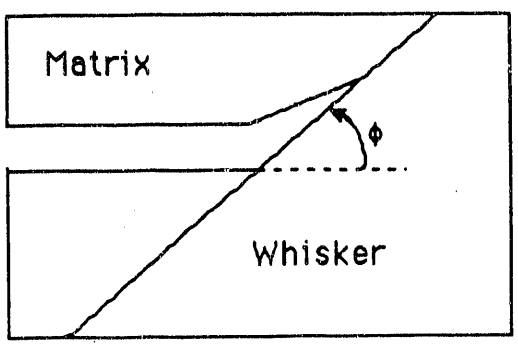

Figure 5. Whisker Orientation for Initial Debonding Along the Interface [76].

The extent of debonding is influenced by residual stresses and the whisker radius. Debonding is typically small when the interface is under residual compression, but can be extensive when the whiskers are smooth.

Continuation of the initial debond along the interface is influenced by additional variables such as residual stress and the whisker radius. Debond growth is most prevalent in the crack wake [78, 79]. For interfaces under residual tension, debonding in the crack wake is unstable and encourages the extensive debonding of smooth whiskers. Debond growth occurs when the stress (t) on the whisker reaches a critical value t^*, given by $t^* \approx 2.2\ E_f e_T$, where E_f is the elastic modulus of the fiber and e_T is the misfit strain. When $t > t^*$, the debond propagates unstably up the interface.

Residual compression and/or irregular whisker morphology causes stable debonding [76]. As in the previous case, a threshold stress must be exceeded before debonds can further propagate in the wake. In this case, when the threshold stress is exceeded, debonding occurs stably, to an extent determined by the friction coefficient along the previously debonded interface (μ) and the residual strain, until $t \rightarrow E_f e_T/\upsilon$ (υ is Poisson's ratio for the whisker), whereupon the interface separates and further debonding occurs unstably.

The steady-state toughening (ΔG_c) imparted by whiskers can be considered to have four essential contributions, as shown in Figure 6, and represented by the following [73]:

$$\Delta G_c/fd \approx S^2/E - Ee_T^2 + 4(\Gamma_i/R)/(1-f) + (\tau/d)\Sigma_i(h_i^2/R) \qquad \{8\}$$

where d is the debond length, R the whisker radius, f the volume fraction, S the whisker "strength", h_i the pullout length, and τ the

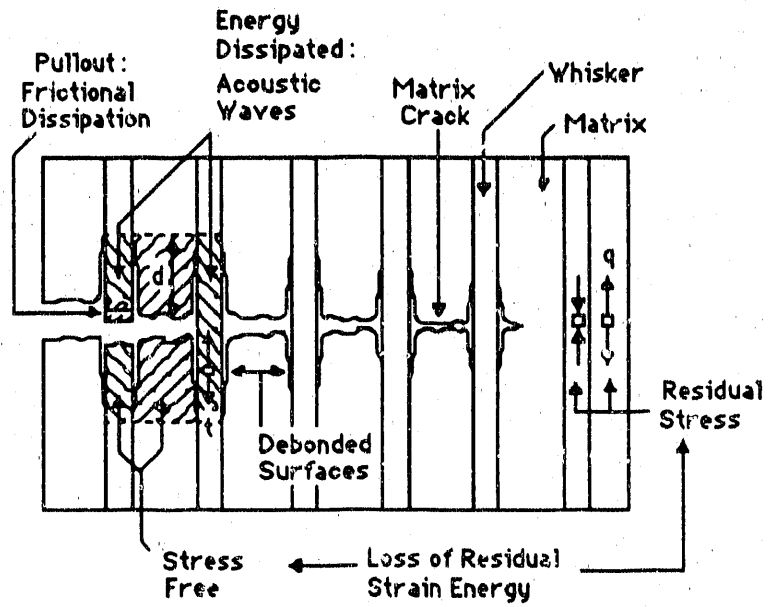

Figure 6. Schematic Indicating the Various Contributions to the Steady-State Toughness [73].

sliding resistance of the debonded surface. The first term (S^2/E) is simply the strain energy stored in the whisker over the debonded length on both sides of the matrix crack before the whisker fails. This strain energy dissipates as acoustic waves, and thus contributes positively to the toughening. The second term (Ee_T^2) is the residual strain energy in each composite element within the debond length, as governed by the misfit strain (e_T). This strain energy is lost from the system when the whisker fails, and thus detracts from the toughness, independently of the sign of e_T. The third term $\{4(\Gamma_i/R)/(1-f)\}$ is the energy needed to create the debond fracture surface, with Γ_i being the fracture energy per unit area, which must be positive. The last term $\{(\tau/d)\Sigma_i(h_i^2/R)\}$ is the pullout contribution, with h_i being the pullout length and τ the sliding resistance of the debonded surface. This term is also positive because heat is generated by the frictional sliding and the interfaces.

The various contributions to toughness represented in the above equation were examined by direct measurements of h, d, R, and f in Al_2O_3-SiC whisker where the interfaces are subject to residual compression and Si_3N_4-SiC whisker composites with interfaces in residual tension [73]. Debond lengths were found to vary between 2R and 6R in the Al_2O_3-SiC whisker composite and R and 3R in the Si_3N_4-SiC whisker composite (R = whisker radius). Observations in the Al_2O_3-SiC whisker indicated the bridging zone size to be about 3 to 4 whisker spacings. Usually the second whisker behind the crack tip was fractured in the Si_3N_4-SiC whisker composites, indicating that the bridging zone was very small. The pullout contribution in both composites was negligible since only a small fraction of whiskers exhibit this phenomenon.

Observations by Campbell *et al.* [73] indicated that nonaligned, inclined whiskers typically fail by bending and do not provide a pullout contribution to toughening. As a consequence, composites with randomly oriented whiskers cannot normally be expected to exhibit high toughness. Given this limitation, a useful increase in toughness is still possible with the major toughening mechanisms being the fracture energy consumed in creating the debonded interface and the stored strain energy in the whiskers at failure which is dissipates as acoustic waves. Thus, enhanced debonding is desirable. The contribution to ΔG_c from the energy of the debonded surfaces is expected to be weakly dependent on the whisker interface energy (Γ_i) and insensitive to whisker radius, but should increase as the whisker strength increases. The bridging contribution, however, should increase appreciably as either Γ_i decreases or the whisker radius increases and should become

the dominant contribution to toughness for small Γ_i and large R, provided that the "strength" (S) is also high. This "strength" of the whiskers is not simply related to the uniaxial fracture strength of the whiskers, and its relation to it is not clearly understood at this time. Campbell *et. al*, [73] also pointed out that while small Γ_i and large S clearly enhance debonding, such variable as residual strain, surface roughness, and friction coefficient could be important in determining the debond length.

Grains can also participate in bridging. Bridging grains can be induced in two ways: grain boundary debonding and residual stress [80, 81]. Low fracture energy grain boundaries can allow debonding, as in whisker reinforced materials, such that toughening involves the same terms described in the equation for ΔG_c given above [82].

Residual stress-induced bridging occurs because circumferential compression causes the crack to circumvent local, highly stressed regions. Evans [82] reports that it has been shown that such a bridging process increases the steady-state toughness according to:

$$\Delta K_c = 2.5 f E \Delta\alpha \Delta T (R)^{1/2} \qquad \{9\}$$

where f is the volume fraction of highly stressed grains that result in bridging elements; $\Delta\alpha$ and ΔT are the changes in thermal expansion and temperature, respectively, and 2R is the grain diameter. This increase in toughness arises because ligament failure occurs unstably and energy is dissipated in this process as acoustic waves, partly negated by some reduction in residual strain energy.

3. Load Transfer

Load transfer from a matrix to high strength fibers is the fundamental basis of polymeric and metal matrix composites. The

extent of toughening due to load transfer generally increases as the ratio of fiber elastic modulus to matrix modulus (E_f/E_m) increases and the volume fraction of fibers increases [83]. The lower limit at which meaningful toughening can be obtained is when $E_f/E_m \approx 2$. Maximum load transfer requires a high volume fraction of unidirectionally aligned fibers. Toughening by load transfer in whisker reinforced composites is possible because of the high elastic modulus of the whisker (500-700 GPa).

The extent of strengthening (and hence toughening) due to load transfer to unidirectional fibers can be estimated by [84]:

$$\sigma_o = \sigma_{mu} \{1 + V_f [(E_f/E_m) - 1]\} \quad \{10\}$$

where σ_o is the stress at which microcracks appear, σ_{mu} is the matrix stress at its breaking strain, E_f and E_m are the elastic modulus of the fiber and matrix, respectively, and V_f is the volume fraction of fibers. The strength of composites reinforced with random discontinuous fibers has not been treated in detail in the literature. However, the variation of the elastic modulus has been investigated and experimental results suggest that the variation in strength correlates well with variations in the modulus [85]. The case of reinforcing with random mats of fibers in both 2 and 3 dimensions has been studied by Cox [86]. He found the increase in modulus of the composite (E) to be affected by $(E_fV_f)/3$ for the in-plane random case and $(E_fV_f)/6$ for the 3 dimensional case. Therefore, the strength increment should be reduced to 1/3 and 1/6 its aligned value for planar and 3 dimensional random orientations, respectively. In the planar case, this is equivalent to assuming that only whiskers with their axes between -30° and +30° away from the applied stress directions contribute to strength

increase. Therefore, the strength increase would be given by the following equation:

$$\sigma_o' = \sigma_{mu} \{1 + (V_f/3) [(E_f/E_m) - 1]\} \quad \{11\}$$

III. EXPERIMENTAL PROCEDURE

A. Processing of Composites

Processing of the composites includes raw material characterization, powder mixing, and composite fabrication by sintering and hot-pressing.

1. Raw Materials Characterization

A fine grain AlN powder[1] was used in the present study. The chemical composition of the powder as given by the manufacturer is listed in Table 7.

Table 7. Chemical Composition of AlN Powder.

Element	Amount (wt%)
Al	balance
N	33.1
C	0.07
O	2
Fe	0.018
other metals	< 0.02

The reported average grain size (FSSS) and surface area (BET) are 1.0 μm and 5.1 m^2/g, respectively. The x-ray diffraction (XRD)[2] indicated AlN as the only phase present. A coarse grain AlN[3] (3-5 μm)

---

[1]Grade C, H. C. Starck, W. Germany.

[2]Rigaku D/Max, Rigaku/USA Inc., Danvers, MA.

[3]Grade A, H. C. Starck, W. Germany.

was used as a protective powder bed during sintering. A β-SiC[4] + 20 wt% graphite powder[5] bed was also used during sintering.

Yttrium oxide (Y_2O_3)[6] was added as a sintering aid. The average particle size (Coulter) and surface area (BET) are 4.2 μm and 9.5 m^2/g, respectively. XRD showed Y_2O_3 to be the only phase present.

β-SiC whiskers[7] were used in this study. No manufacturer data about the whiskers was given. Figure 7 is a scanning electron microscope (SEM) micrograph of the SiC whiskers as received from the manufacturer. The average whisker is ≈ 0.5 μm in diameter and 20-100 μm in length. Generally the whiskers had a smooth surface; however, a very small fraction of the whiskers had stacking defects observable by SEM.

XRD indicated the presence of β-SiC with a small amount of α-SiC. Whisker surface chemistry was analyzed by x-ray photoelectron spectroscopy (XPS).[8] XPS analysis showed the surface to be rich in silica. Impurities of N (≈ 4.3 at%) and Ca (≈ 0.71 at%) were detected.

2. Powder Mixing

Because of potential health hazards from inhaling SiC whiskers, the manufacturer would not make large quantities of whiskers available for batch processing, but they agreed to mix the composition batches themselves. They suggested 3 wt% Y_2O_3 as a sintering aid and

---

[4]Grade B10, H. C. Starck, F. R. Germany.

[5]Grade #38, Fisher Scientific Co., Fair Lawn, NJ.

[6]Grade 5600, Molycorp, White Plains, NY.

[7]Grade F9, Advanced Composite Materials Corp., Greer, SC.

[8]Model PHI 5400, Perkin Elmer/Physical Electronics Div., Eden Prairie, MN.

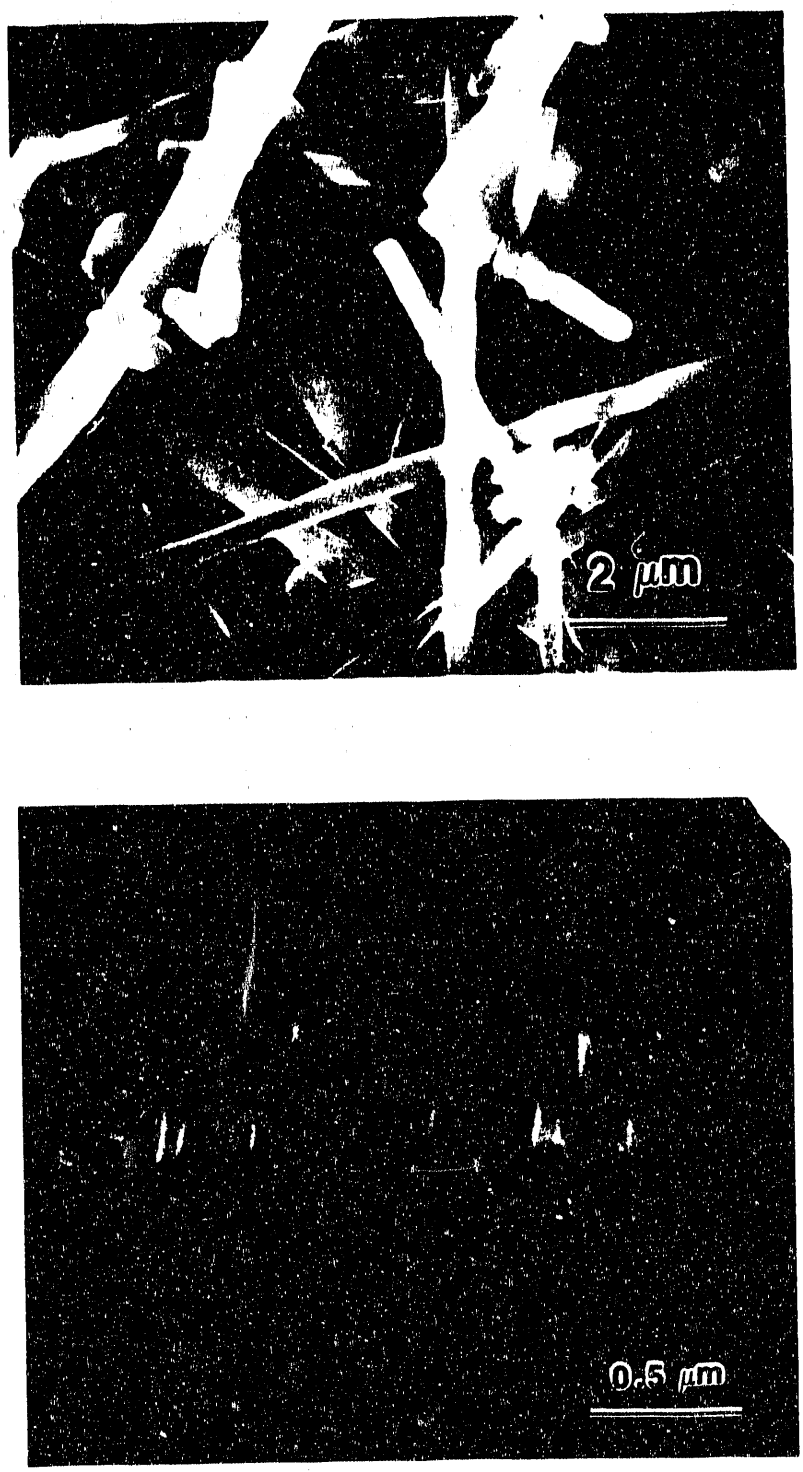

Figure 7. Silicon Carbide Whiskers as Received From the Manufacturer.

10 vol% SiC whiskers (composition designated as A3Y10W) as a composition that, from a preliminary investigation, hot-pressed to full density [87]. Batch compositions of 0 and 3 wt% Y_2O_3 and 0-10 vol% whiskers were mixed by wet ball milling (8-16 hrs) in denatured methyl alcohol in a plastic jar using plastic media. After milling the alcohol was dried by evaporation, and the batch was dry milled (≈ 30 min) to break agglomerates. This resulted in a fine powder mixture. A 20 vol% SiC whisker batch (A3Y20W) was mixed by using the A3Y10W batch as a base composition and increasing the SiC whisker content. The 20 vol% SiC whisker batch was then mixed under conditions similar to those batches mixed by the whisker manufacturer. Figure 8 is an SEM micrograph of the composite starting powder. The average AlN powder size is 1-2 μm, although some large agglomerates up to ≈ 10 μm could be seen. Figure 8 shows the aspect ratios (length to diameter ratio) of the 10 and 20 vol% SiC whisker batches to be 20-50 and 15-30, respectively.

3. Composite Fabrication

Pellets for pressureless sintering were formed and cold isostatically pressed[9] at a pressure of 172 MPa. Pressureless sintering was done in a tungsten resistant heated furnace[10] at 1700°-1800°C under 0.5 atm Ar with the pellets packed in a protective powder bed in a graphite crucible with a lid. The lid was not sealed tight. Temperature was monitored by a type C thermocouple (W-Re).

---

[9]Autoclave Engineers Inc., Erie, PA.

[10]Model 300-MC, Thermal Technology/Brew Div., Concord, NH.

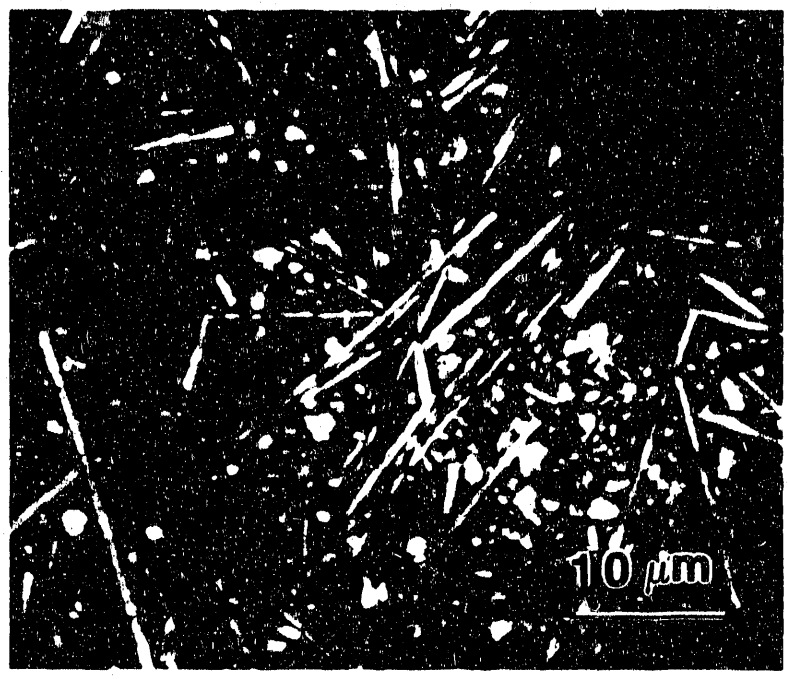

a

b

Figure 8. SEM Micrograph of the Mixed Starting Powder.
(a) 10 Vol% SiC Whiskers.
(b) 20 Vol% SiC Whiskers.

Hot-pressing[11] was done in a graphite die, 3.81 cm in diameter, lined with Grafoil[12] under a pressure of 27.6 MPa at 1600°-1800°C in either vacuum or 0.5 atm Ar atmosphere. The temperature was controlled using a two color infrared pyrometer focused on the outside of the die wall. The times and temperatures used in sintering and hot-pressing the samples are shown in Table 8.

B. Composite Characterization

1. Property Measurement

Physical and mechanical properties of the composites were measured. These include fluid displacement density measurements, elastic moduli measurements using a pulse echo ultrasound technique, and fracture toughness measurements using the indentation technique.

(a) Density. Composite densities were measured using the Archimedes principle of fluid displacement. Pressureless sintered samples were cleaned using an abrasive unit[13] to remove any adhering powder from the protective powder bed during sintering. Sintered samples were typically ground prior to density measurement, and hot-pressed samples were cut from the hot-pressed billets using a low speed diamond saw.[14] All samples were weighed on an electronic balance[15] to ± 0.002 g.

---

[11]30 ton vacuum hot-press, GVA Corp./Vacuum Industries Div., Somerville, MA.

[12]GTA-5 mil, Union Carbide, Carbon Products Div., Cleveland, OH.

[13]Model-K, S. S. White Abrasive Unit/Pennwalt, Piscataway, NJ.

[14]Isomet Low-Speed Saw, Buehler, Lake Bluff, IL.

[15]Mettler PJ 300, Hightstown, NJ.

Table 8. Composite Processing Parameters.

Processing Conditions	Sample Composition			
	A3Y	A3Y10W	A3Y20W	A0Y10W
PL 1800°C, 4 hr	X	X		
PL 1800°C, 2 hr	X	X		
PLH 1800°C, 2 hr, no powder bed	X	X	X	
PL 1800°C, 2 hr, no powder bed	X	X	X	
PL 1800°C, 2 hr, SiC+C powder bed	X	X	X	
PL 1800°C, 0.5 hr	X	X		
PL 1750°C, 2 hr	X	X		
PL 1750°C, 1 hr		X		
PL 1750°C, 0.5 hr		X		
PL 1700°C, 2 hr	X	X		
HP 1600°C, 1 hr, vac	X	X		
HP 1700°C, 1 hr, vac	X	X		X
HP 1800°C, 0.5 hr, 0.5 atm Ar	X	X	X	X

A3Y = AlN + 3wt% Y_2O_3 A3Y10W = AlN + 3wt% Y_2O_3 + 10% whiskers
A3Y20W = AlN + 3% Y_2O_3 + 20% whisker A0Y10W = AlN + 10% whiskers

HP = hot-pressed PL = pressureless sintered
PLH = pressureless sintered in the hot-press
AlN powder bed used, unless otherwise stated.

Sample density was calculated using the following formula:

$$\text{Density} = (\text{dry wt.} \times \text{density of liquid})/(\text{dry wt.} - \text{suspended wt.}) \quad \{12\}$$

with samples suspended in toluene. Low densities showed weight changes with time while suspended due to the saturated of toluene associated with open porosity. The densities of these samples were measured from weight and dimensions of ground samples.

(b) Elastic Moduli. Elastic moduli were measured by the pulse echo technique [88] on the as-processed hot-pressed billets using a commercial ultrasonic testing system.[16] Sample thickness was

[16]NDT-150, Nortec Inc., Kennewick, WA.

measured to the nearest 0.01 mm using a micrometer. The billet surfaces were nearly parallel with thickness varying only ± 0.01 mm over the ultrasonic transducer contact area. The longitudinal and shear wave velocities of the sample were determined by measuring the round-trip time of travel of an ultrasonic pulse (1-5 MHz frequency) between the transducer and the back of the sample. Pulse time travel was measured to the nearest 0.1 μsec using a calibrated oscilloscope by observing the time between reflections of the initial pulse.

Longitudinal wave measurements and shear wave measurements were made using a compressional wave transducer and a shear wave transducer, respectively. Both transducers were ≈ 1.4 mm in diameter and coupled to the sample using a commercial coupling agent.[17] The equations for calculating the shear modulus and Young's elastic modulus are given below:

The longitudinal wave speed (c_1) is given by:

$$c_1 = (2t)/t_1 \qquad \{13\}$$

where t is the sample thickness and t_1 is longitudinal time. The shear wave speed (c_2) is given by:

$$c_2 = (2t)/t_2 \qquad \{14\}$$

where t_2 is the shear time. The shear modulus (G) is given by:

$$G = \rho c_2^2 \qquad \{15\}$$

where ρ is the sample density. Poisson's ratio (υ) is given by:

$$\upsilon = [2-(t_2/t_1)^2]/2[1-(t_2/t_1)^2] \qquad \{16\}$$

Young's elastic modulus (E) is given by:

$$E = 2(1+\upsilon)G \qquad \{17\}$$

---

[17]SWC Coupling Agent, Panametrics, Waltham, MA.

(c) Indentation Fracture Toughness. Sample fracture toughness was measured using the indentation technique with a Vickers diamond point indenter. Samples approximately 0.5 cm x 1 cm x 0.2 cm thick were cut from hot-pressed billets using a low-speed diamond saw. Surfaces perpendicular to the hot-press direction were ground parallel and polished[18] to a 1 μm finish with diamond paste.

Indentation measurements were made using a commercial hardness tester[19] fitted with an ocular measuring scale. Approximately ten indentations were made at loads of 7 kg (68.6 N) and 8 kg (78.4 N). Since the calculated fracture toughnesses at each load were nearly identical, the crack length measurements for both loads were added together to determine K_{IC}. The fracture toughness in $Pa \cdot m^{1/2}$ was calculated using two equations. The first equation was proposed by Lawn and Fuller [65]:

$$K_{IC} = [1/(\pi^{3/2} \tan \psi)]P/c^{3/2} \quad \{4\}$$

where ψ equals 68° for a Vickers indenter, P is the indentation load (N) and c is the crack length (m). The second equation was proposed by Anstis *et al.* [67]:

$$K_{IC} = 0.016(E/H)^{1/2}P/c^{3/2} \quad \{5\}$$

where E is Young's modulus (GPa) and H is the hardness (GPa). Figure 9 shows a typical Vickers Indentation in the hot-pressed 20 vol% SiC whisker composite. The cracks are well behaved and emanate from the four corners of the indentation. All indentations showed that the condition for validity of the above equations was met, i.e., $c \geq 2a$. In

---

[18]Ecomet III with Automet attachment, Buehler, Lake Bluff, IL.

[19]Model 3212.01, Zwick, Mark V Laboratory Inc., East Granby, CT.

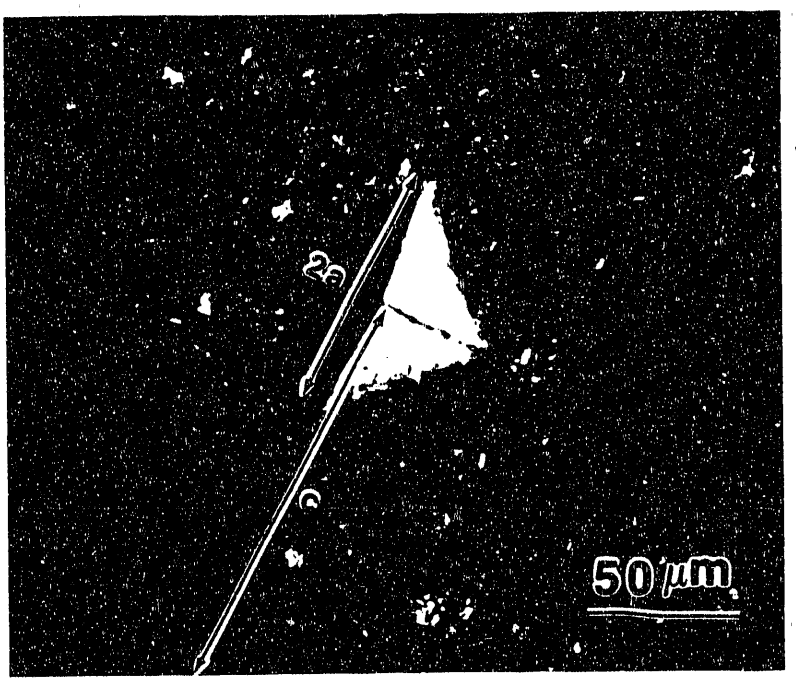

Figure 9. A Typical Vickers Indentation in the 20 Vol% Whisker Hot-Pressed Composite Showing the $c \geq 2a$.

order to calculate K_{IC} using the second equation, the ratio of E/H is needed. The ratio of E/H was determined by indentation using a Knoop diamond point indenter according to the following equation [68]:

$$H/E = (0.141-b'/a')/0.45 \quad \{7\}$$

where a' and b' are the short and long dimensions of the residual Knoop impression, respectively.

C. Microstructure and Microchemistry

Microstructural and microchemical characterization included powder x-ray diffraction of raw materials and composites, scanning electron microscopy of fracture and indentation surfaces, and transmission electron microscopy with and without energy dispersive x-ray analysis of the composites.

1. X-ray Diffraction

Powder x-ray diffraction (XRD)[20] with a Cu x-ray source and a Ni filter was used to determine the crystalline phases in the raw materials and fabricated samples. X-ray diffraction samples were prepared from composites by sectioning with a low speed diamond saw, and were generally ground to a 30 μm to 15 μm surface finish. Powder and whisker samples were made by packing the powder into the x-ray sample holder against a glass slide.

2. Scanning Electron Microscopy

Powder particle size, whisker morphology and aspect ratio, composite fracture surfaces, and interaction of Vickers induced cracks with the microstructure were observed by high resolution scanning

[20]Rigaku D/Max, Rigaku/USA Inc., Danvers, MA.

electron microscopy (SEM).[21] Powder and whisker samples were prepared by placing a drop of a powder/whisker-acetone slurry onto an aluminum stub. After the dispersion dried, the powder/whiskers were coated with carbon using a conventional evaporator.[22] Fracture surfaces were obtained by manually fracturing thin samples. Fracture and indentation samples were mounted on aluminum stubs using colloidal graphite[23] and coated with carbon.

3. Transmission Electron Microscopy

Transmission electron microscopy (TEM)[24] was used to study the composite microstructure and microchemistry using ultra-thin window (UTW) energy dispersive spectroscopy (EDS). Samples for TEM were prepared by cutting slices about 100 μm thick and mechanically polishing[25] down to 80-90 μm thick with a final polish of 3 μm diamond paste. Three millimeter disks were then cut using an ultrasonic disk cutter[26] and dimple ground[27] with 3 μm diamond paste to a thickness of 40-50 μm. Final thinning of the sample was performed by argon ion milling[28] to perforation at a voltage of 6 kV and

---

[21]Hitachi S-800, Hitachi Ltd., Tokyo, Japan.

[22]Model KDTG-3P, New York Air Brake Co./Kinney Vacuum Div., Boston, MA.

[23]DAG 154, Acheson Colloids Company, Port Huron, MI.

[24]Philips EM-420, equipped with EDS from EDAX International Inc., Prairie View, IL, and Philips CM-12, electron microscopes, Philips Instruments Inc., Eindhoven, the Netherlands.

[25]Minimet, Buehler, Lake Bluff, IL.

[26]Model 601, Gatan Inc., Pleasanton, CA.

[27]Model 656 precision dimple grinder, Gatan Inc., Pleasanton, CA.

[28]Model 600 dual ion mill, Gatan Inc., Pleasanton, CA.

1 mA beam current and a gun tilt of 15-25°. A thin coating of carbon on the samples eliminated any charging problems.

IV. RESULTS AND DISCUSSION

A. Density and Phase Composition

Table 9 lists the processing conditions used to fabricate the composites, along with the measured density and percent of theoretical density. Measured densities of hot-pressed (HP) samples were often greater than that estimated by using the weight fractions of AlN, Y_2O_3, Al_2O_3, and SiC and their respected densities. These values were attributed to the presence of a number of minor phases. Accurate values of density would require the knowledge of the volume fraction and crystal structure of all minor phases, which were not available. Therefore, an approximate correction of theoretical density values was performed, based on the assumption that HP A3Y samples (1600°C and 1800°C) were fully dense (100%) and that all samples with 3 wt% Y_2O_3 contained similar types and amounts of minor phases.*

In general the density increased with temperature and holding time. Full density was achieved for A3Y hot-pressed at 1600°C for 1 hr, but decreased to ≈ 92% with the addition of 10 vol% SiC whiskers (A3Y10W). Hot-pressing at 1700°C for 1 hr resulted in full density for A3Y10W and 96% for the 10 vol% SiC whisker composite without Y_2O_3 (A0Y10W). Hot-pressing at 1800°C for 0.5 hr resulted in a slight drop in density for the A3Y10W composite due to the shorter holding time, however full density for A0Y10W (≈ 99%) was obtained under these

---

* The types and amounts of minor phases were found to vary depending upon processing conditions, as will be mentioned later. However, the above mentioned correction was still used.

Table 9. Densities of Fabricated Samples

Composition	Processing Conditions*	Theoretical Density (g/cm^3)	Measured Density (g/cm^3)	Corrected Theoretical Density (g/cm^3)	Percent of Corrected Theoretical Density
A3Y	HP 1800°C, 0.5 hr, 0.5 atm Ar	3.320	3.39	3.380	100
	HP 1600°C, 1 hr, vac	3.320	3.37	3.380	100
	PL 1800°C, 4 hr	3.320	3.28	3.380	94.7
	PL 1800°C, 2 hr	3.320	3.23	3.380	94.4
	PL 1800°C, 0.5 hr	3.320	3.29	3.380	97.3
	PLH 1800°C, 2 hr, no pb	3.320	3.28	3.380	97.0
	PL 1800°C, 2 hr, no pb	3.320	3.23	3.380	95.6
	PL 1800°C, 2 hr, SiC+C pb	3.320	3.21	3.380	95.0
	PL 1750°C, 2 hr	3.320	3.25	3.380	96.2
	PL 1700°C, 2 hr	3.320	2.30	3.380	68.0
A3Y10W	HP 1800°C, 0.5 hr, 0.5 atm Ar	3.309	3.32	3.369	98.5
	HP 1700°C, 1 hr, vac	3.309	3.40	3.369	100
	HP 1600°C, 1 hr, vac	3.309	3.11	3.369	92.3
	PL 1800°C, 4 hr	3.309	3.21	3.369	95.3
	PL 1800°C, 2 hr	3.309	3.15	3.369	93.5
	PL 1800°C, 0.5 hr	3.309	3.22	3.369	95.6
	PLH 1800°C, 2 hr, no pb	3.309	3.14	3.369	93.2
	PL 1800°C, 2 hr, no pb	3.309	3.15	3.369	93.5
	PL 1800°C, 2 hr, SiC+C pb	3.309	3.08	3.369	91.4
	PL 1750°C, 2 hr	3.309	3.15	3.369	93.5
	PL 1750°C, 1 hr	3.309	2.85	3.369	84.6
	PL 1750°C, 0.5 hr	3.309	2.20	3.369	65.3
	PL 1700°C, 2 hr	3.309	2.61	3.369	77.5
A3Y20W	HP 1800°C, 0.5 hr, 0.5 atm Ar	3.298	3.29	3.357	98.0
	PLH 1800°C, 2 hr, no pb	3.298	2.27	3.357	67.6
	PL 1800°C, 2 hr, no pb	3.298	2.38	3.357	70.9
	PL 1800°C, 2 hr, SiC+C pb	3.298	2.00	3.357	59.6
A0Y10W	HP 1700°C, 1 hr, vac	3.278	3.15	3.278	96.1
	HP 1800°C, 0.5 hr, 0.5 atm Ar	3.278	3.24	3.278	98.8

A3Y = AlN + 3% Y_2O_3 A3Y10W = AlN + 3% Y_2O_3 + 10% whiskers
A3Y20W = AlN + 3% Y_2O_3 + 20% whisker A0Y10W = AlN + 10% whiskers

HP = hot-pressed PL = pressureless sintered
PLH = pressureless sintered in hot-press
*AlN powder bed (pb) used, unless otherwise stated.

conditions. A density of 98% was measured for the 20 vol% SiC whisker composite (A3Y20W) when hot-pressed at 1800°C for 0.5 hr.

The addition of 10 vol% SiC whiskers did not hinder densification by pressureless sintering (PL). Densities of 95-97% were measured for sintered A3Y samples, while A3Y10W samples had densities of 93-95%. However, composites containing 20 vol% SiC whiskers could not be sintered to densities above ≈ 70%. These observations are consistent with those made by Tiegs and Becker [9] where it was observed that Al_2O_3-SiC whisker composites could be sintered to high densities ($\geq$95% theoretical) when the whisker loading was $\leq$10 vol%. Above 10 vol% the density decreased dramatically and sintered materials without closed porosity were obtained. They concluded that in order to fabricate dense composites from powder with high whisker contents, some type of encapsulation (for hot-isostatic pressing) and pressure assistance appeared to be required.

The type of protective powder bed used during sintering also affected the sample density. Generally, samples sintered in an AlN powder bed [$PL_{(PB=AlN)}$] or without a powder bed [$PL_{(NO\ PB)}$] had higher densities than those samples sintered in a β–SiC + 20 wt% C (graphite) powder bed [$PL_{(PB=SiC+C)}$]. This was due to the relative amount of oxygen impurity within the samples with higher oxygen amounts resulting in higher densities. Specific effects of the powder bed on sample density and microstructure are discussed later.

The phase composition of the samples was investigated by XRD. Table 10 lists the phases present in A3Y10W samples; these phases were, however, present in all samples under the same conditions. Minor phases identified include yttrium-aluminum-garnet (YAG) and γ-

aluminum oxynitride (γ-AlON). All samples containing Y_2O_3 showed the presence of YAG. The composition without Y_2O_3 (A0Y10W, not shown in Table 10) showed only γ-AlON. Little or no γ-AlON was identified below 1800°C, consistent with the appearance of γ-AlON above ≈ 1700°C in the AlN-Al_2O_3 system [2.1.2-20]. The sample sintered at 1800°C for 4 hours showed no γ-AlON. This is most likely due to extensive reaction between phases found in this sample, which will be mentioned later. The XRD of SiC is also discussed later.

Table 10. Phase Composition of A3Y10W Composites.

Processing Conditions	Phases Present			
	AlN	SiC	YAG	ALON
PL 1800°C, 4 hr	Y	N	Y	N
PL 1800°C, 2 hr	Y	N	Y	Y
PLH 1800°C, 2 hr, no powder bed	Y	Y	Y	Y
PL 1800°C, 2 hr, no powder bed	Y	N	Y	Y
PL 1800°C, 2 hr, SiC+C powder bed	Y	Y	Y	Y
PL 1800°C, 0.5 hr	Y	trace	Y	Y
PL 1750°C, 2 hr	Y	N	Y	trace
HP 1700°C, 1 hr, vac	Y	Y	Y	N
HP 1800°C, 0.5 hr, 0.5 atm Ar	Y	Y	Y	Y

HP = hot-pressed PL = pressureless sintered
PLH = pressureless sintered in the hot-press
AlN powder bed used, unless otherwise stated.

B. Microstructure

1. General Features

Figure 10 shows typical areas within HP composites. Preferential orientation of the SiC whiskers was observed in TEM and confirmed by XRD in HP samples. Whiskers in TEM thin foils prepared

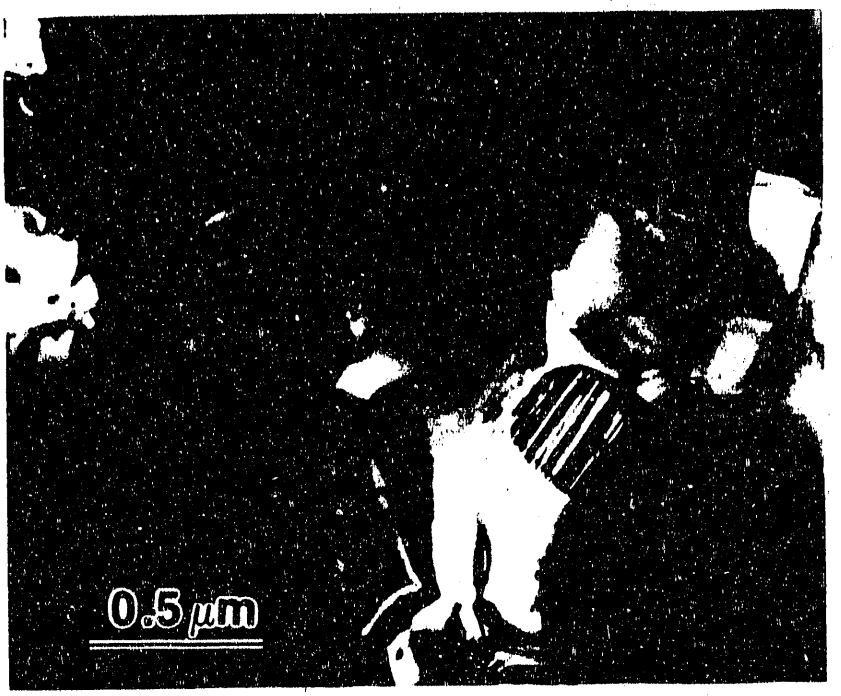

a

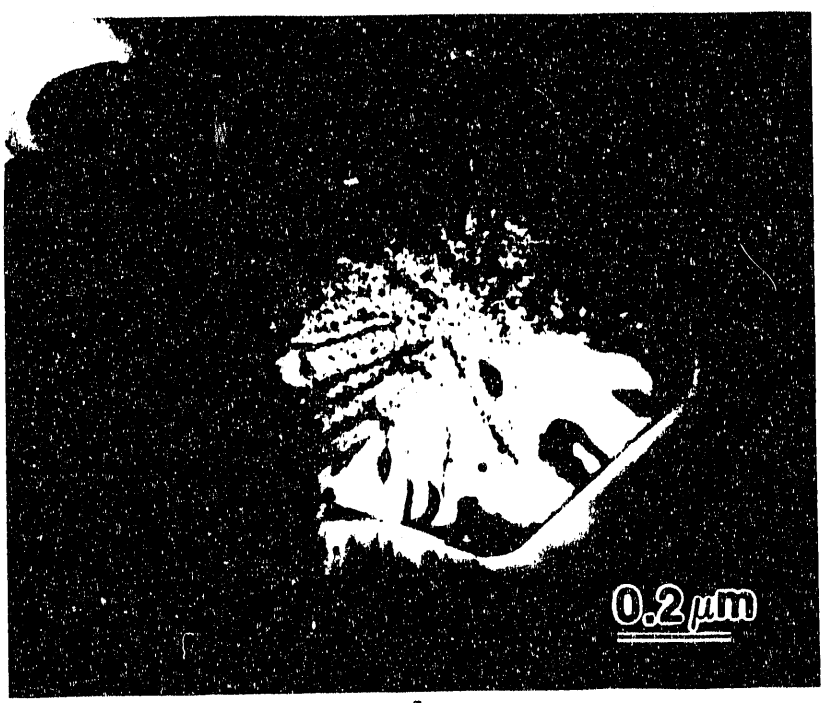

b

Figure 10. (a) TEM Micrograph of a Typical Area in HP Composites.
(b) Cross-section of a SiC whisker.

from planes perpendicular to the HP direction were observed to lie within the sample plane, while thin foils oriented parallel to the HP direction showed whiskers in cross-section. Stacking faults, dislocations, and inclusions within SiC whiskers are also clearly seen by TEM.

Whiskers were usually observed in grain boundaries as shown in Figure 11, but a small number of whiskers were found embedded within single AlN grains. Minor phases, such as YAG, were usually found near SiC whiskers in grain boundaries. Porosity was also observed at grain boundaries and along SiC whiskers. Fracture surfaces of AlN grains observed by SEM show predominantly intergranular fracture, both in monolithic AlN and in the AlN-SiC whisker composites. Whisker pullout was observed in the composites as shown in Figure 12. Matrix grain growth was observed with increased sintering time as seen in Figure 13. The grain size was estimated from SEM and TEM to be ≈ 2 μm for HP samples.

2. Oxygen Content

The type of protective powder bed used during sintering, as well as the type of furnace affected the oxygen content of the samples. The oxygen content was qualitatively measured in the TEM using UTW EDS. Initially, sintering was performed in a refractory metal furnace with compacts embedded in an AlN powder bed. This was done to create a self-stabilizing atmosphere and limit AlN decomposition from the samples. Sintering AlN in an AlN powder bed is a common practice [3,31,35-37,42].

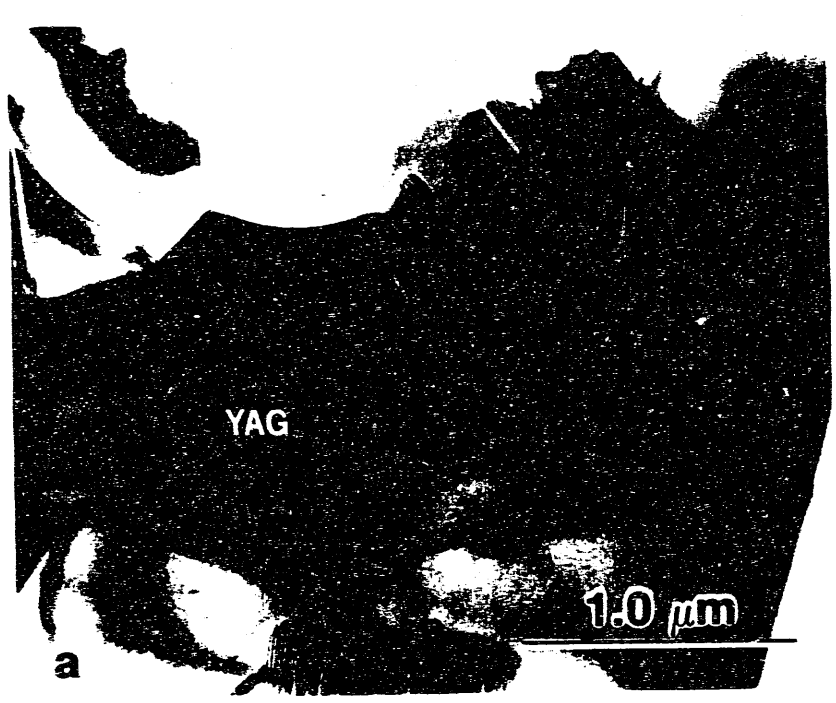

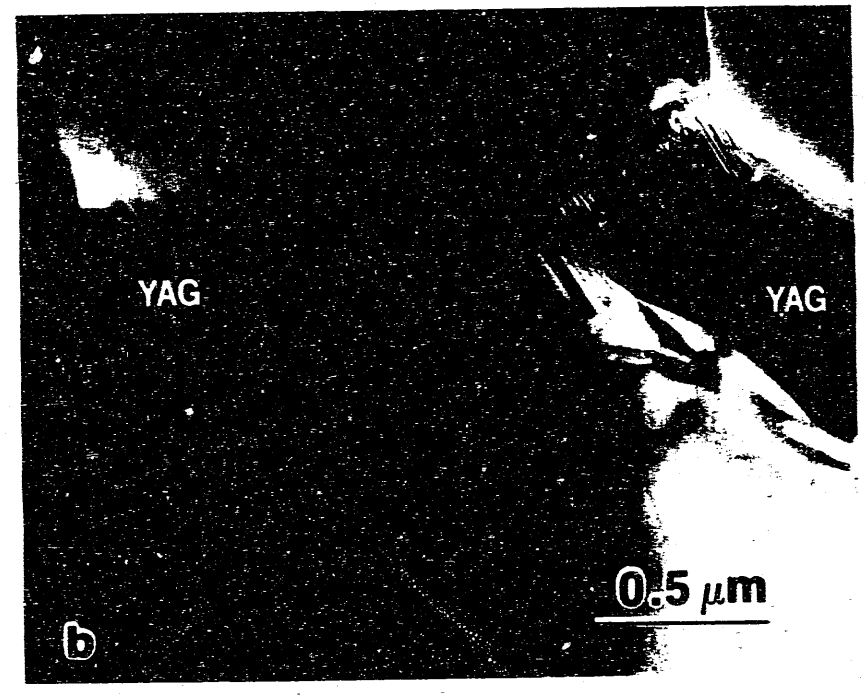

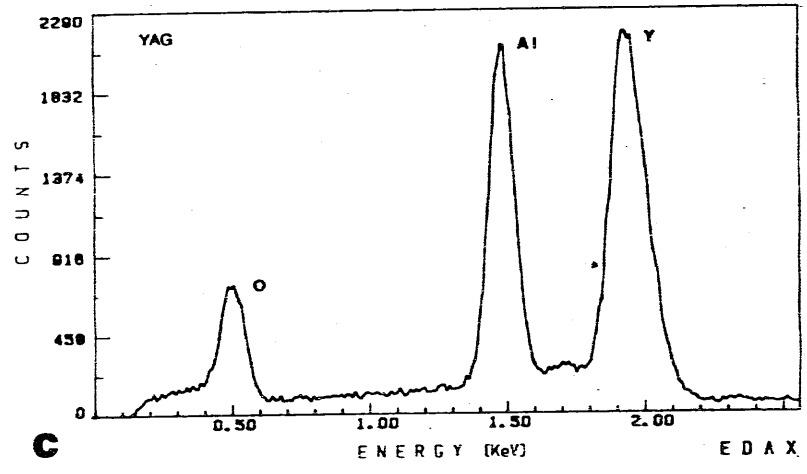

Figure 11. TEM Micrographs of the YAG Phase Near SiC Whiskers (a,b). (c) is the UTW EDS Spectrum of the Phase in (a) ; a Similar Spectrum was Obtained for (b). (A3Y10W $PL_{(PB=AlN)}$ 1800°C, 0.5 hr)

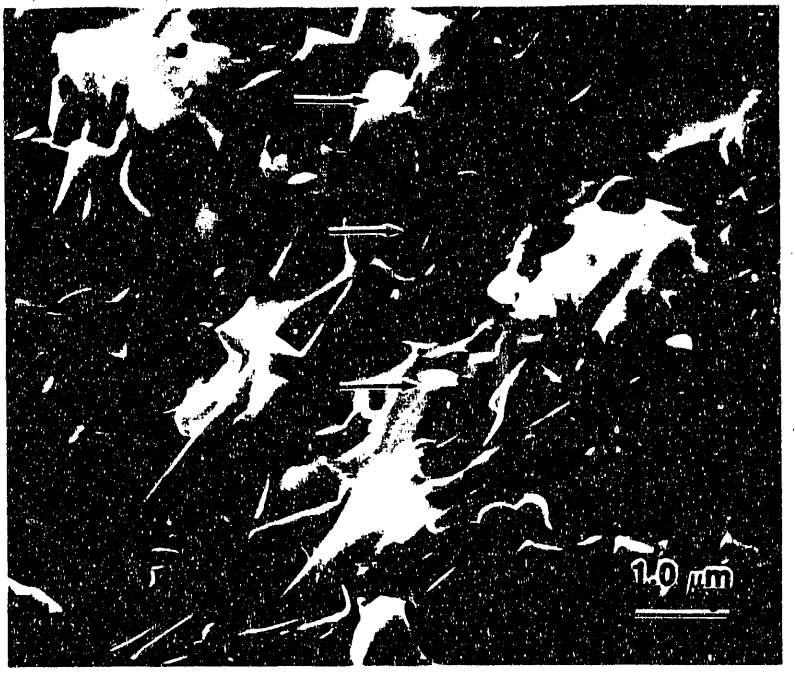

Figure 12. Fracture Surface of A3Y20W HP 1800°C Sample Showing Whisker Pullout (arrows).

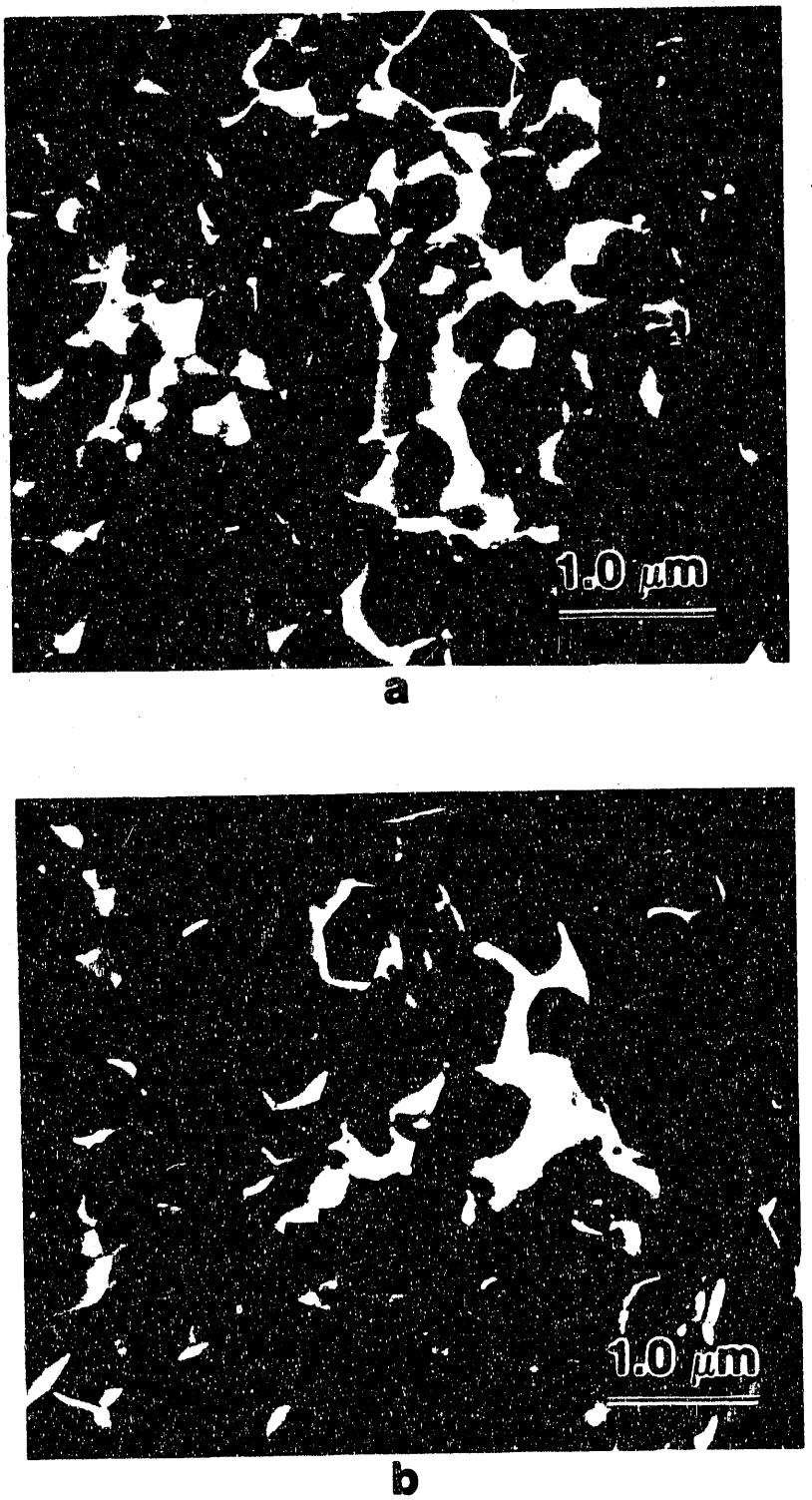

Figure 13. Fracture Surface Showing Matrix Grain Growth.
(a) A3Y10W PL 1800°C 2hr in an AlN Powder Bed.
(b) A3Y10W PL 1800°C 4hr in an AlN Powder Bed.

A very high oxygen content was observed in [$PL_{(PB=AlN)}$] samples as shown in Figure 14. The high Si peaks are also significant as discussed later. Oxygen most likely comes from the decomposition of AlN in the powder bed. A measured weight loss (≈ 1-2 %) and the formation of small, light blue colored crystals on the inside surface of the graphite crucible indicate decomposition of the powder bed. Crystals matching this description were identified by Foster *et al.* [44] as aluminum oxycarbide (Al_2OC) and were reported to form when AlN was sintered in furnaces containing graphite. The composition of the crystals observed in the present study was not checked, but they are thought to be Al_2OC.

The oxygen content of samples sintered without a powder bed [$PL_{(NO\ PB)}$] was not measured. From results discussed later it will be shown that these samples also had a high oxygen content. However, the PLH samples, which were sintered in the hot-press without a powder bed, showed only a small oxygen peak. This was due to a better vacuum in the hot-press than in the refractory metal furnace before back filling with Ar gas. This effectively lowered the oxygen content within the furnace.

The oxygen content could be reduced during pressureless sintering by substituting a β-SiC + 20 wt% C (graphite) powder bed for the AlN powder bed or no powder bed. Figure 15 shows the relatively low oxygen content of the [$PL_{(PB=SiC+C)}$] sample. The oxygen is lower in these samples compared to the $PL_{(PB=AlN)}$ samples because the oxygen impurity can react with the carbon powder to form CO. Additionally, the oxygen impurity of the SiC powder (< 1 wt%) is less than that of the AlN. Carbon powder was not added to the AlN powder bed in order to avoid the formation of Al_2OC.

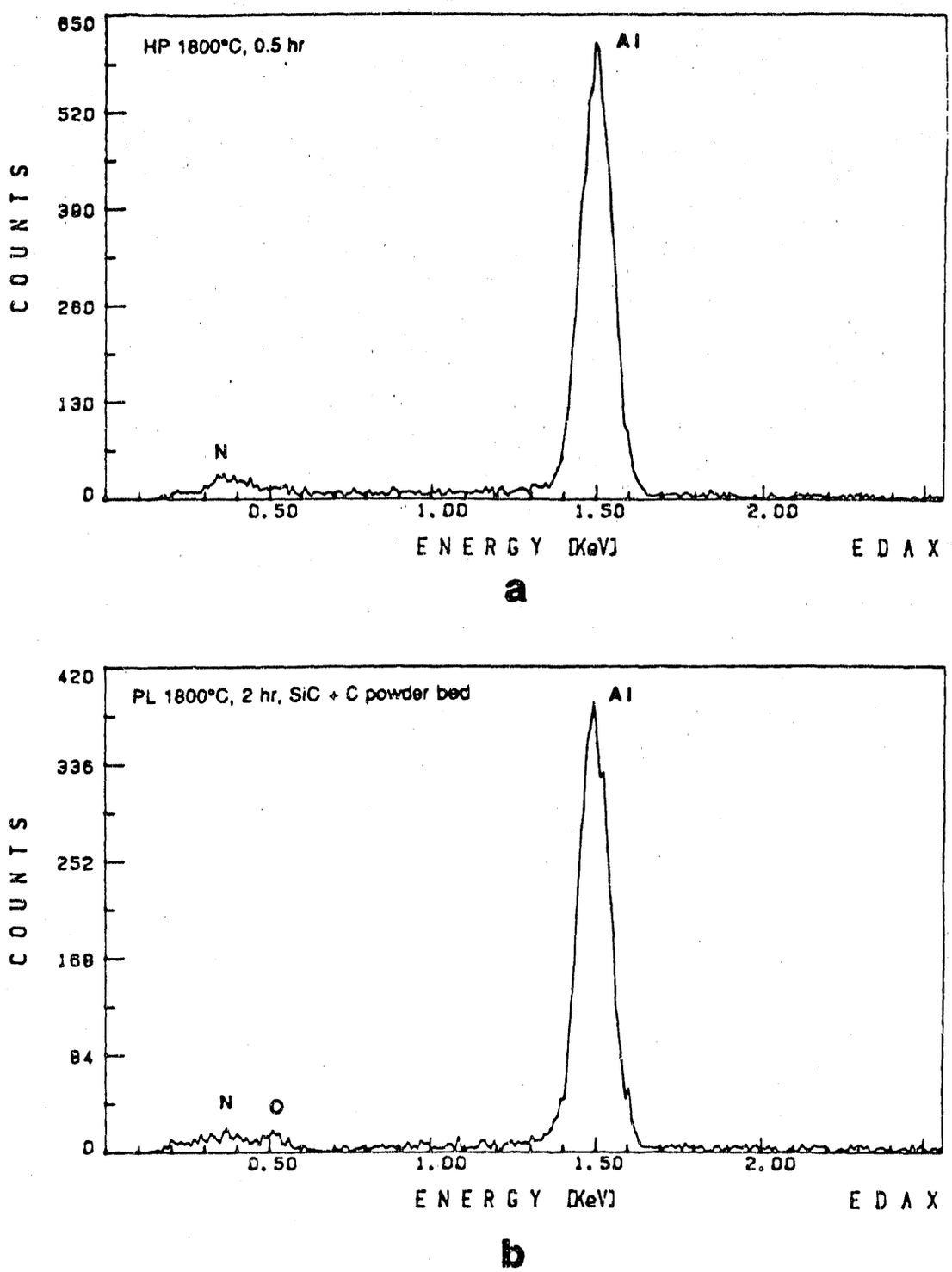

Figure 15. EDS Measurements Showing a Low Oxygen Content.
(a) Hot-Pressed Composite.
(b) Sample Sintered in a Protective Powder Bed.

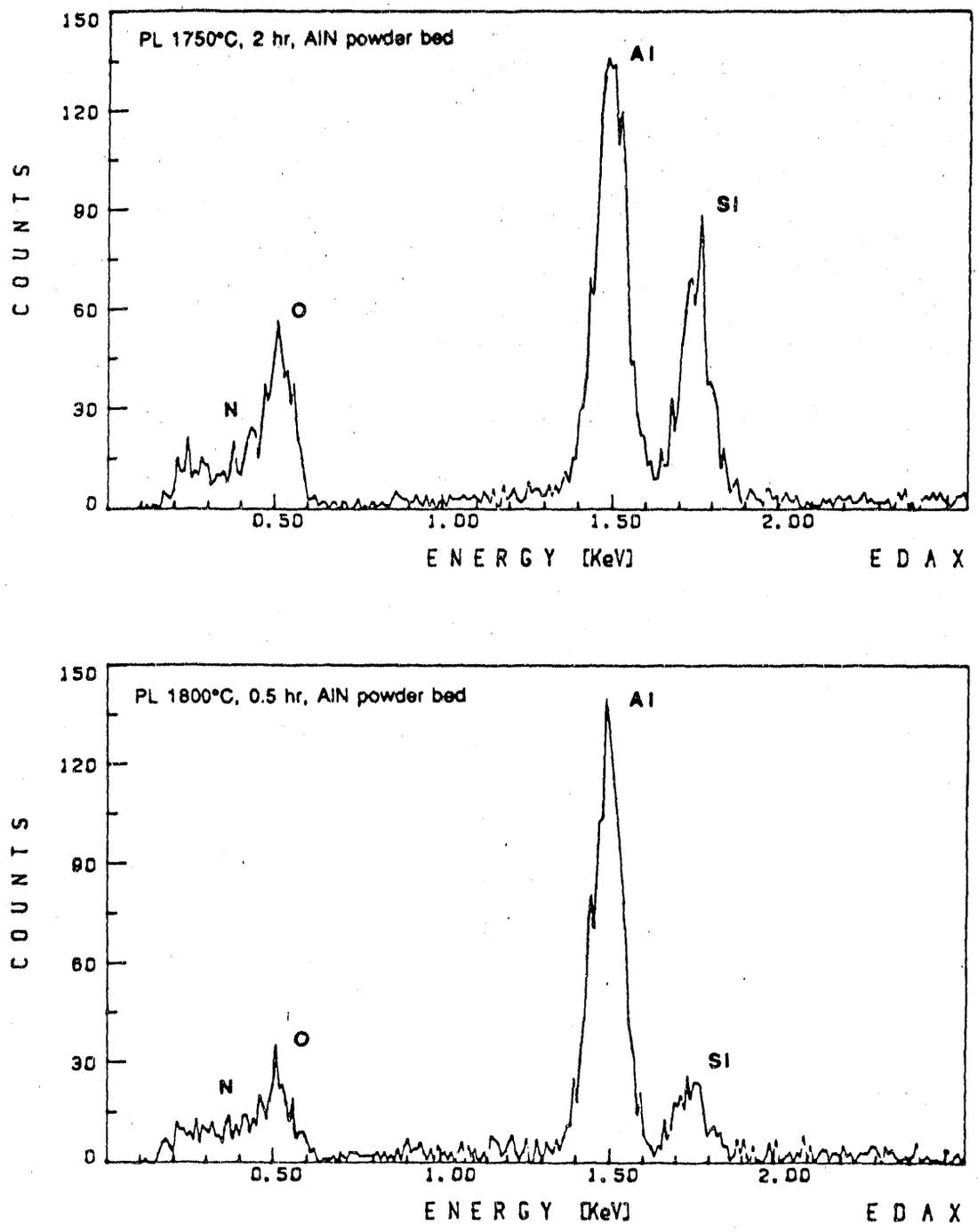

Figure 14. EDS Measurements Showing a High Oxygen Content in the Matrix of Pressureless Sintered Samples.

Also shown in Figure 15 is a HP sample. No oxygen was detected in any HP samples because the applied pressure during hot-pressing would tend to force the oxygen impurity out of the sample.

C. Stability of SiC Whiskers

1. X-Ray Diffraction of SiC

Table 10 (page 41) shows the relationship between the processing conditions and the observance of SiC peaks by XRD. The low oxygen content samples (HP, $PL_{(PB=SiC+C)}$, and PLH) all show the presence of SiC. No SiC was detected in $PL_{(PB=AlN)}$ samples unless the sintering time was kept very short (1800°C, 0.5 hr). No SiC was detected in the $PL_{(NO\ PB)}$ samples indicting they also contained a high oxygen content as alluded to earlier.

The XRD results indicate that the SiC whiskers can degrade. This is also seen in the EDS measurements where Si is be detected in high oxygen samples (see Figure 14). These Si peaks were measured in areas without SiC whiskers; therefore, the Si peak is not due to a nearby whisker. Conversely, samples low in oxygen show little or no Si. The occurrence of a high oxygen peak and a Si peak suggests that SiO_2 is present, conceivably from the oxidation of SiC whiskers. Although a SiO_2 layer was not observed around the SiC whiskers by TEM, whisker degradation products formed by the reaction of SiO_2 with the sintering additives were observed.

2. Reaction of SiC with Matrix and Additives

The reaction of SiC with the sintering additives is clearly seen in the high oxygen $PL_{(PB=AlN)}$ samples as shown in Figure 16. Here a phase containing Y_2O_3 and Al_2O_3 (Area B) has surrounded an area rich in Si

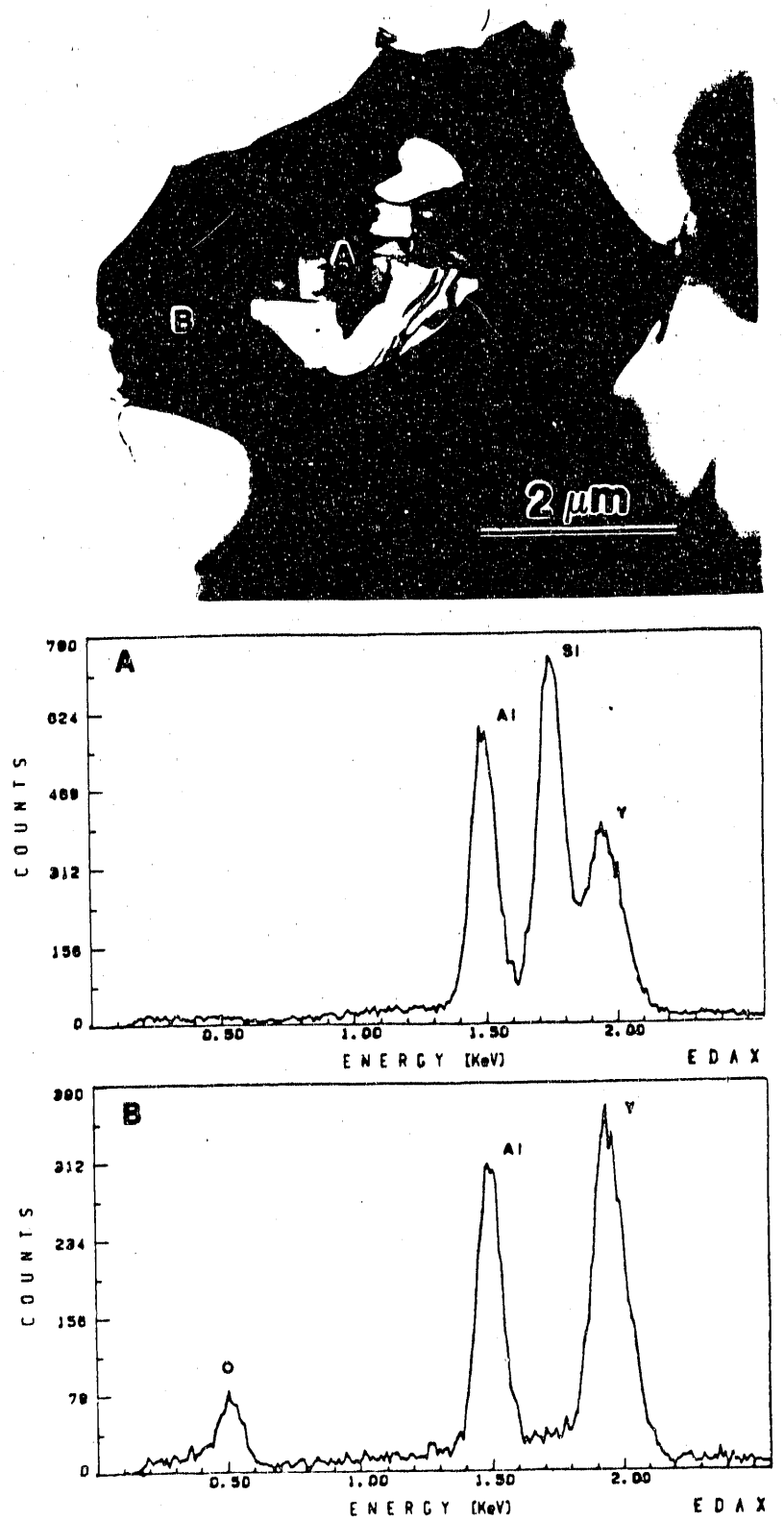

Figure 16. Reaction of SiC with Sintering Additives. (A3Y10W $PL_{(PB=AlN)}$ 1800°C, 2 hr)

(SiO_2) (Area A). Remnants of SiC whiskers are often seen at grain boundaries and triple points, as shown in Figure 17. EDS showed these to contain Y, Al, Si.

Three types of reaction product phases were observed by selected area diffraction (SAD) and EDS, as shown in Figures 18 and 19, respectively. The products were a yttria-alumina-silica glassy phase (a) and two crystalline phases. One of the crystalline phases contained Y and Si (b) and was identified by d-spacing as α-$Y_2Si_2O_7$. The other crystalline phase contained Y, Al, and Si and has a hexagonal crystal structure (c), but could not be positively identified by SAD. However, the EDS spectra suggests Y_2SiAlO_5N ($Y_2O_3 \cdot AlN \cdot SiO_2$) as a possible formula.

In the low oxygen content samples, there was no evidence of reaction between the whiskers and the minor phases by high resolution electron microscopy (HREM). Figure 20 is representative of the YAG-SiC whisker interface in HP and $PL_{(PB=SiC+C)}$ samples. The interface in these samples is clean and the 0.74 nm lattice spacing of the YAG is clearly observed.

Evidence of reaction in a sample that had high oxygen but still contained SiC whiskers was sought. Figure 21 shows the YAG-SiC whisker interface in $PL_{(PB=AlN)}$, sintered at 1800°C for 0.5 hr. There is no clear evidence for reaction, although the interface does look rougher than that in Figure 20. Samples which showed no SiC by XRD were not investigated by HREM because only remnants of SiC whiskers existed in areas too thick for HREM.

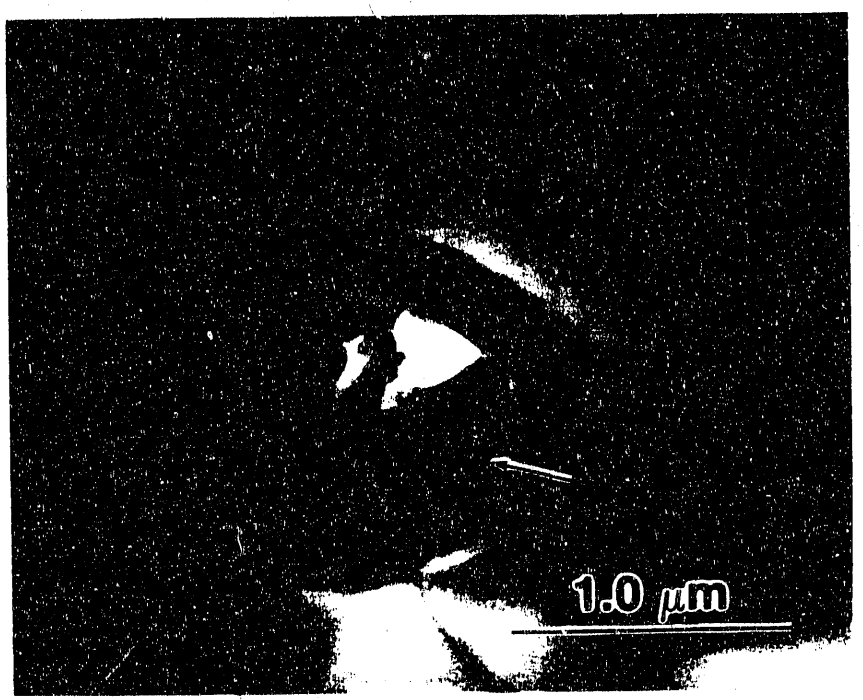

Figure 17. Remnant of SiC whisker in Triple Point (arrow). (A3Y10W Composite $PL_{(PB=AlN)}$ 1800°C, 4 hr)

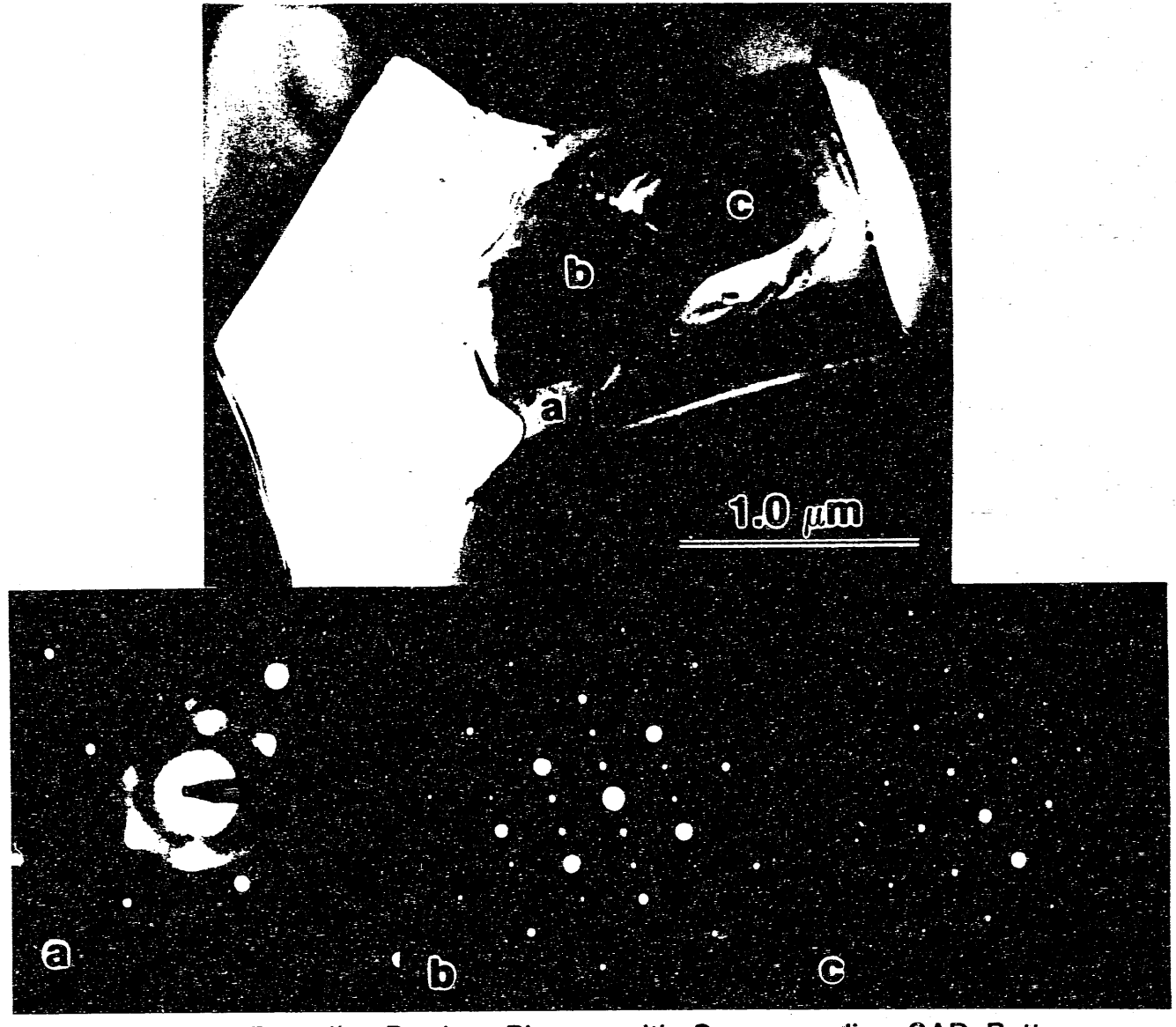

Figure 18. Reaction Product Phases with Corresponding SAD Patterns.
(A3Y10W $PL_{(PB=AIN)}$ 1800°C, 2 hr)

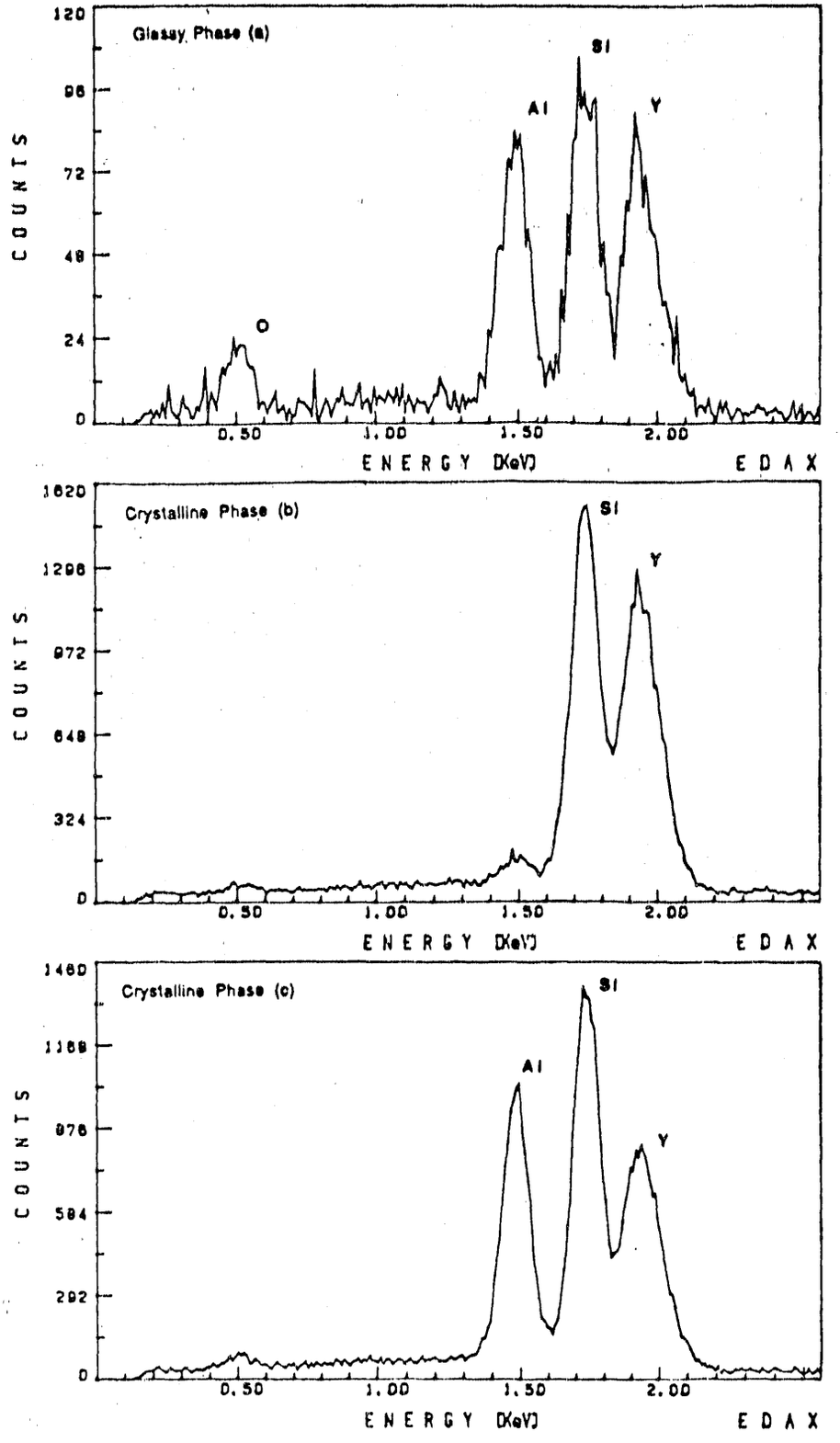

Figure 19. EDS of Reaction Product Phases Shown in Figure 18.

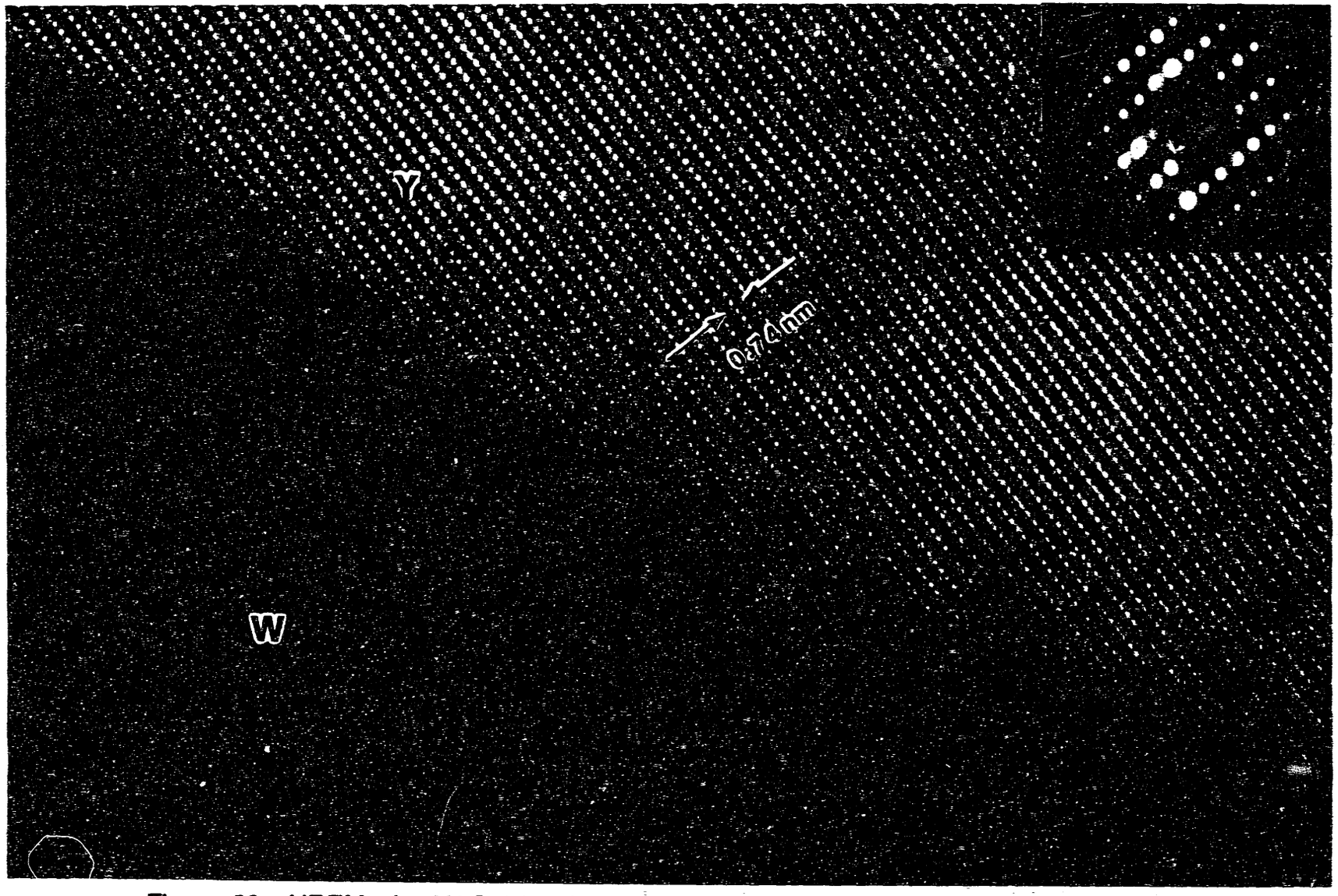

Figure 20. HREM of a YAG (Y) - SiC Whisker (W) Interface in a Low Oxygen Sample. (A3Y10W HP 1800°C, 0.5 hr)

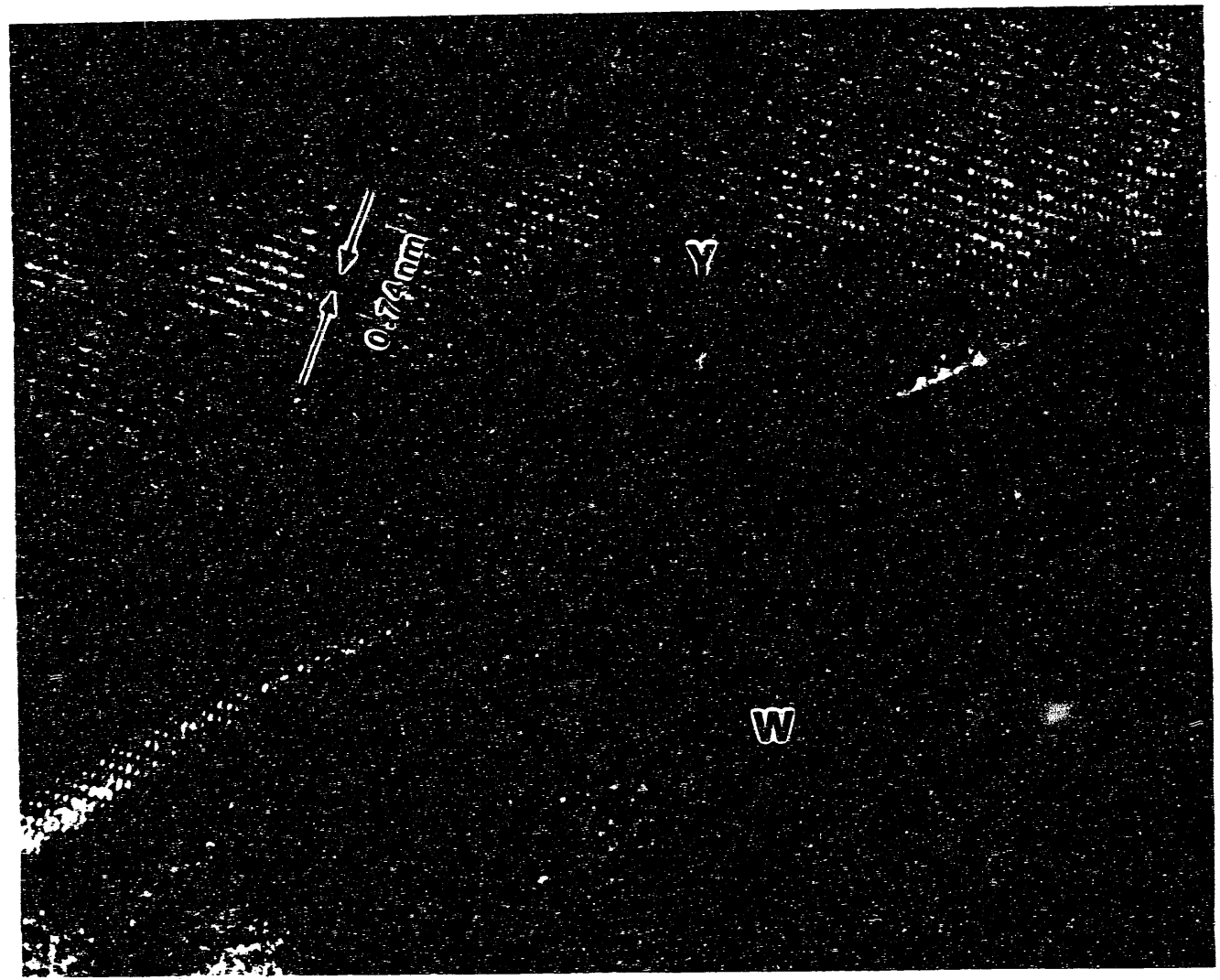

Figure 21. HREM of a YAG (Y) - SiC Whisker (W) Interface in a High Oxygen Sample. (A3Y10W $PL_{(PB=AIN)}$ 1800°C, 0.5 hr)

The variation in the amount of the minor phases in samples can be clearly seen by SEM in Figure 22. Extensive grain boundary phase exists in the $PL_{(PB=AlN)}$ samples (a), while little or no boundary phase is observed in the HP or $PL_{(PB=SiC+C)}$ samples (b). This accounts for the decreased density of the $PL_{(PB=SiC+C)}$ sample compared to the $PL_{(PB=AlN)}$ sample. This grain boundary phase should contain Si (based on TEM/EDS results), but due to its small size it could not be analyzed by EDS in the SEM.

Further evidence of whisker degradation is seen in fracture surfaces viewed in the SEM. Figure 23 shows that whisker morphology is unchanged in HP samples from that of the raw material; the whisker surface is smooth, confirming no degradation. Whisker morphology has degraded slightly in the $PL_{(PB=SiC+C)}$ sample; the surface is no longer as smooth, as shown in Figure 24 (a). Similar whisker morphology was observed in PLH samples. In these samples, there are a large number of whiskers. This is in contrast to $PL_{(PB=AlN)}$ and $PL_{(NO\ PB)}$ samples, where the number of whiskers was very low. Those whiskers that were observed possess a very jagged morphology, as seen in Figure 24 (b).

3. Formation of SiC-AlN Solid Solution

Although no evidence for reaction between the whiskers and additives exists in the $PL_{(PB=SiC+C)}$ sample, Figure 24 shows that the morphology of the whiskers has changed. This is due to solid solution formation between the SiC whisker and AlN. Evidence of solid solution formation is given by HREM and EDS measurements of SiC diffusion into AlN grains.

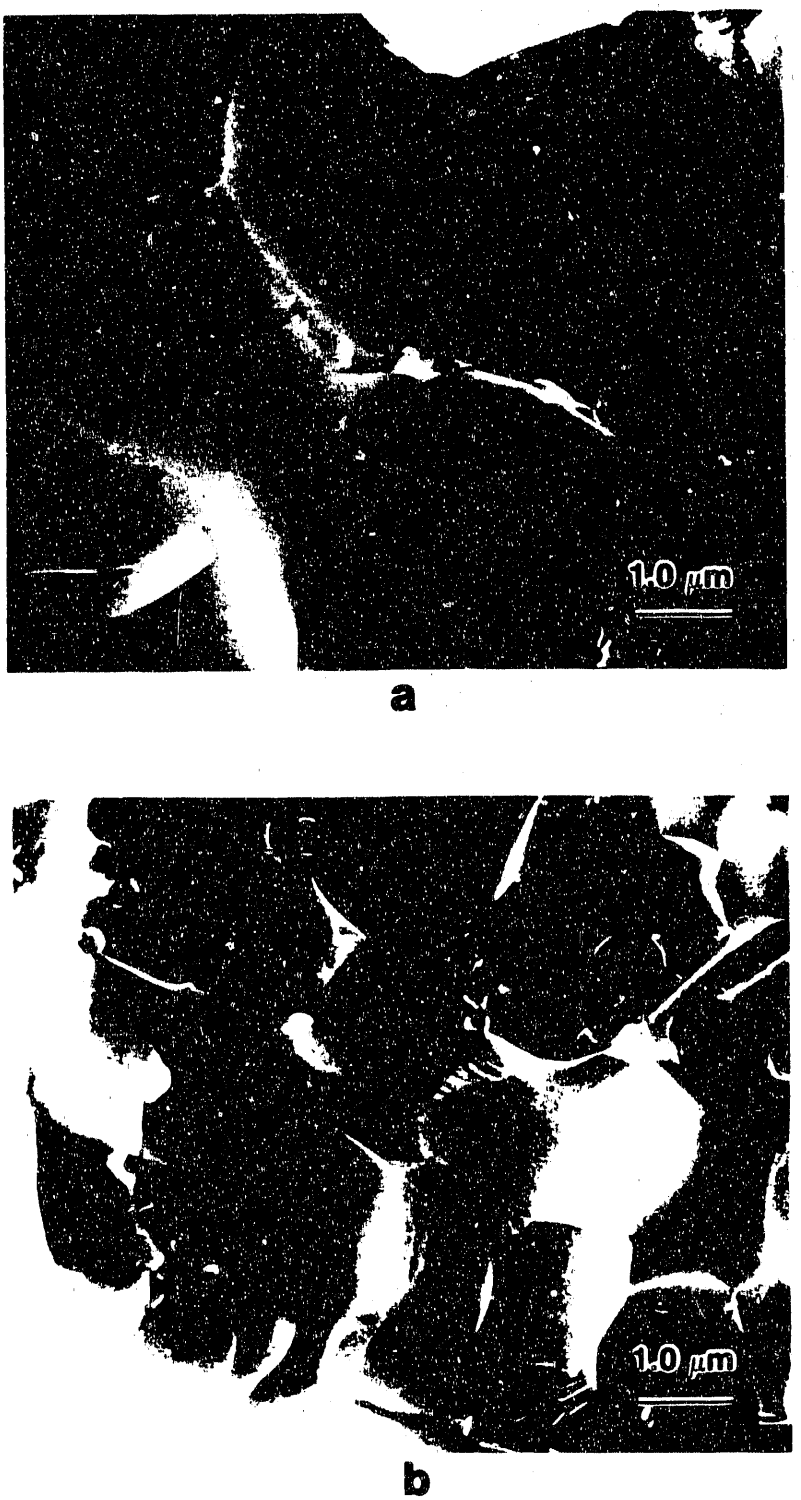

Figure 22. SEM Micrograph Showing the Relative Amount of Minor Phases in A3Y10W Composites Sintered at 1800°C, 2 hr.
(a) High Oxygen Sample [$PL_{(PB=AlN)}$]
(b) Low Oxygen Sample [$PL_{(PB=SiC+C)}$]

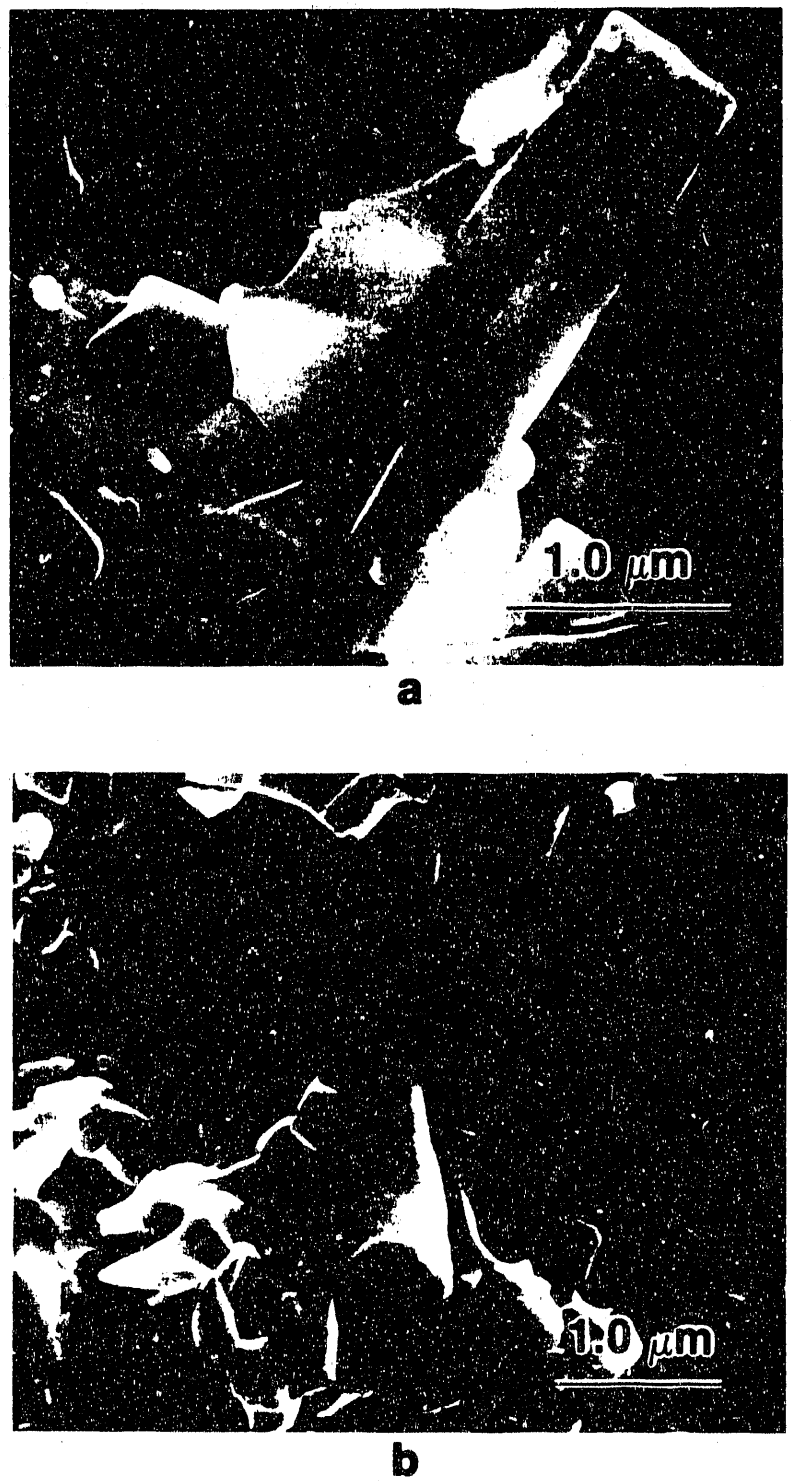

Figure 23. Fracture Surface of A3Y10W HP Composites. No Whisker Degradation is Seen.
(a) HP 1700°C, 1 hr
(b) HP 1800°C, 0.5 hr

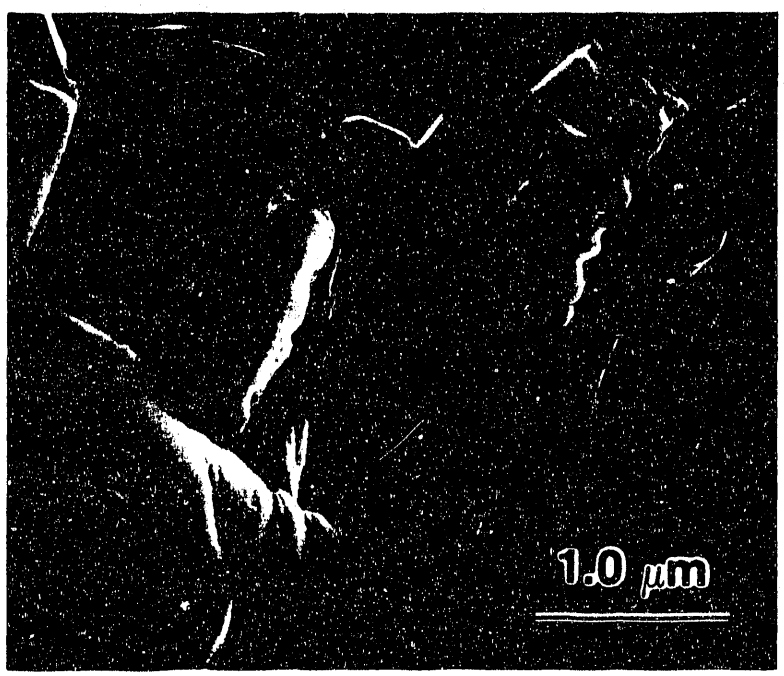

a

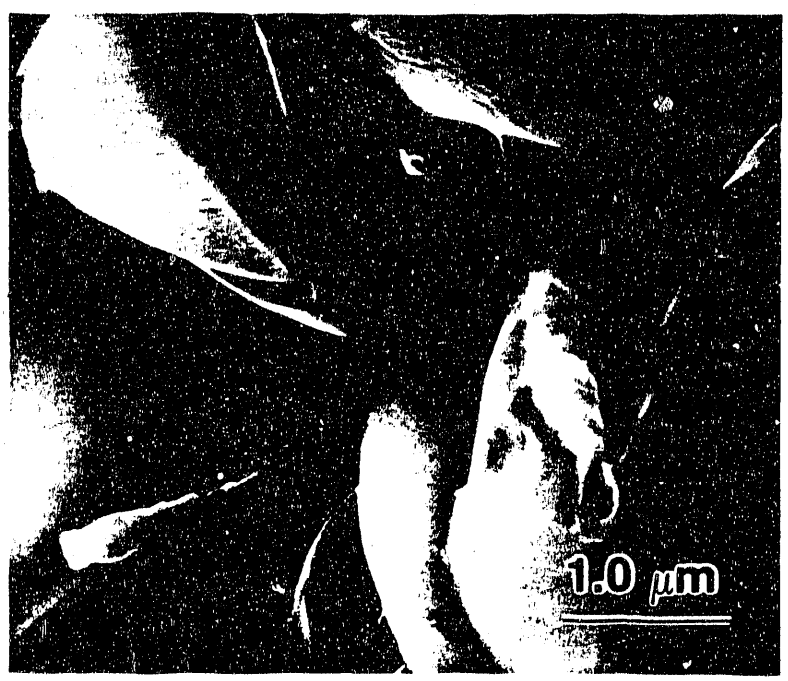

b

Figure 24. SEM of A3Y10W Composites Sintered at 1800°C, 2 hr.
(a) Slight Whisker Degradation is Seen in the Low Oxygen Sample.
(b) Extensive Whisker Degradation is Seen in the High Oxygen Sample.

Figure 25 is a high resolution micrograph of an AlN-SiC whisker interface in the $PL_{(PB=SiC+C)}$ sample, which shows whisker degradation. There is no evidence of a reaction layer, nor was there any contrast change near the interface when the sample was tilted, both of which suggest solid solution formation.

The extent of SiC diffusion into AlN was measured along the indicated line in Figure 26. The amount of Si/(Si+Al) and, therefore, SiC/(SiC+AlN) decreases from a value of 9 at% at a distance of ≈ 0.2 μm to a value of 6.5 at% at a distance of ≈ 1.2 μm. The amount of SiC observed in the AlN grains (6-9 at%) is consistent with the proposed phase diagram for the SiC-AlN system [2.3-3], where a solid solution is predicted at 1800°C for a composition of 90 mol% AlN and 10 mol% SiC. The Si content at distances less than ≈ 0.2 μm was not measured in order to avoid error due to beam spread. Distances greater than ≈ 1.2 μm were also not measured because of intersection with grain boundaries or other whiskers.

A diffusion distance of > 1μm is ≈ 6 times the expected value of ≤ 0.2 μm at 1800°C, as extrapolated from data by Zangvil and Ruh [2.3-5]. Possibly the increased diffusion distance is due to the addition of Y_2O_3 and the formation of a liquid phase during sintering, which would aid in diffusion. However, there was no evidence of minor phases near the SiC whiskers where these measurements were made.

No Si was measured in AlN grains in the HP samples, even at a distance of 0.2 μm. The interface in HP samples shows no whisker degradation, as seen in Figure 27. Evidently, the 0.5 hr hot-pressing time at 1800°C was not long enough to permit extensive diffusion,

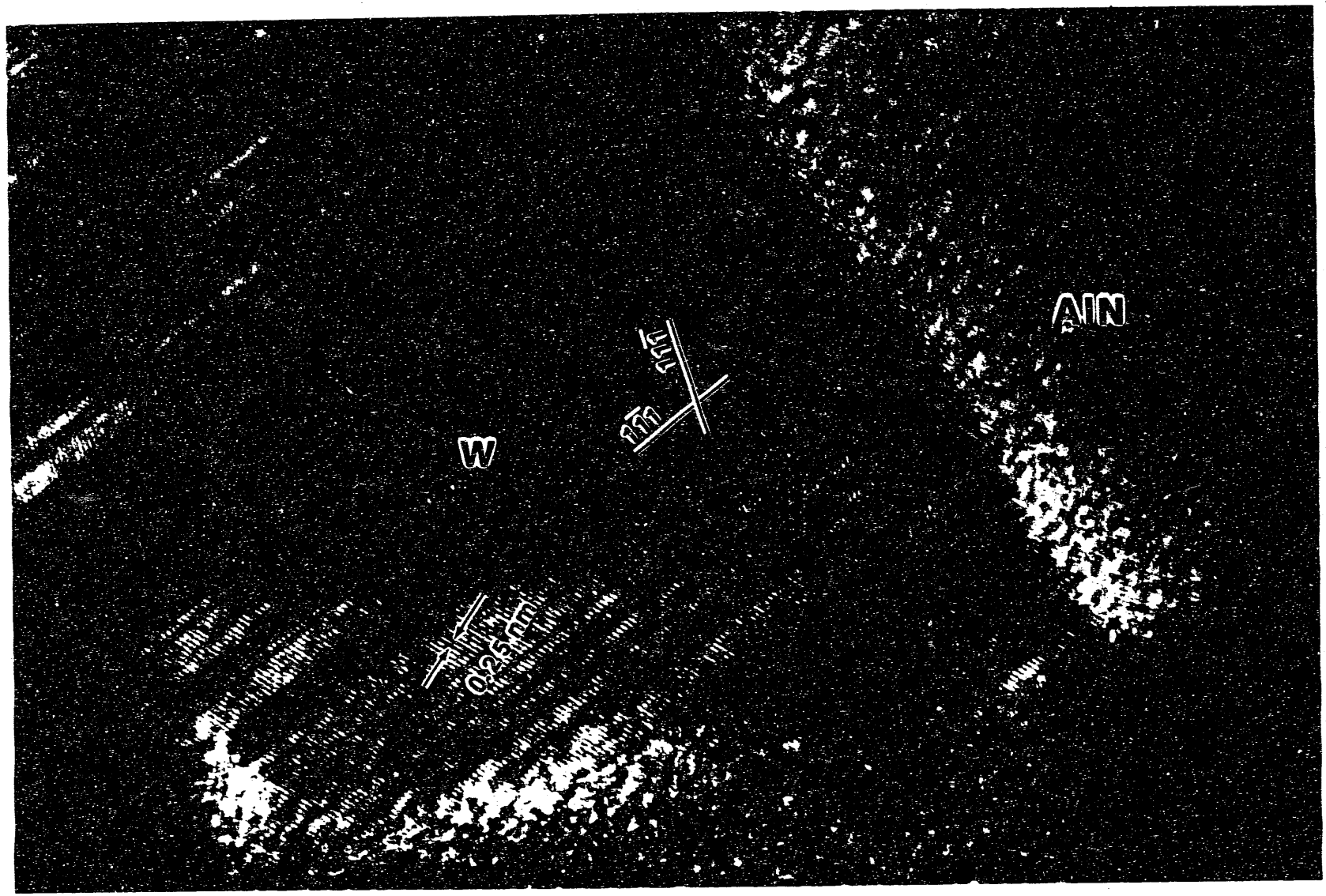

Figure 25. AlN - SiC Whisker Interface Showing Evidence of Solid Solution Formation. The SiC Whisker Exhibits Twinning on a (111) Plane. Z.A. = [011].

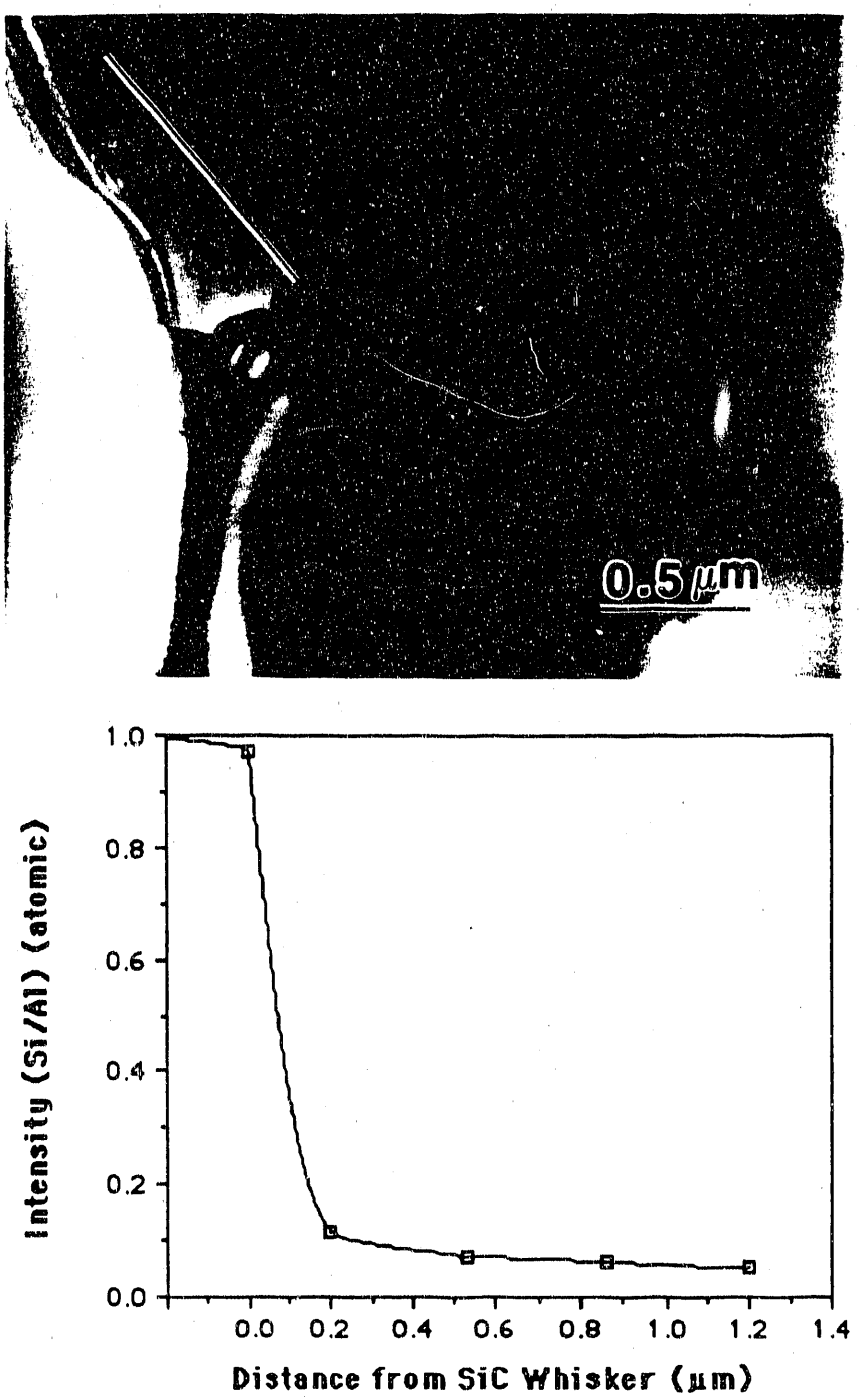

Figure 26. Measurement of SiC Diffusion into AlN. (Measurements Were Made Along the Indicated Line)

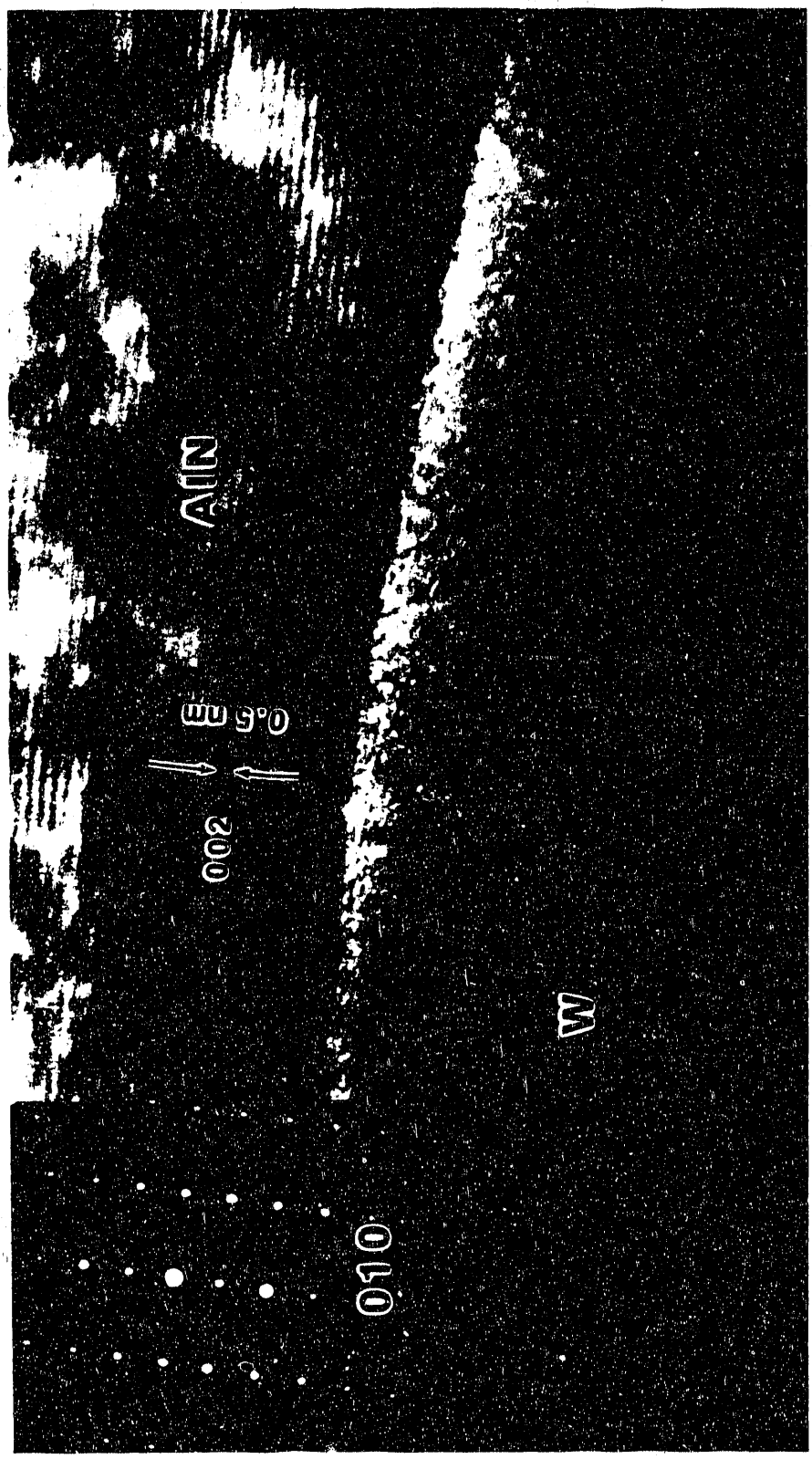

Figure 27. A Typical AlN - SiC Whisker Interface in HP Composites. (A3Y10W HP 1800°C, 0.5 hr)

despite the formation of a liquid phase. If solid solution exists in the HP samples, the diffusion distance is < 0.2 μm and could not be accurately measured.

The diffusion of SiC into AlN could not be accurately measured in high oxygen containing samples because of a background level of Si/Al ≈ 0.085 throughout the sample. However, evidence of solid solution in these samples comes from the morphology of whiskers which are embedded within AlN grains. Figure 28 shows that embedded whiskers have a very irregular morphology; sometimes whole segments of the whisker have disappeared. Because there is contact between the whisker and the AlN grain, the irregular whisker morphology is most likely due to solid solution formation. Irregular whisker morphology was not seen in the HP samples, confirming limited diffusion.

D. Property Measurement

Because the SiC whiskers in HP samples were not degraded, the elastic moduli and fracture toughness of these samples were measured.

1. Elastic Modulus

The elastic modulus was measured by an ultrasonic pulse echo technique [88]. Table 11 lists the elastic moduli as a function of SiC whisker content. A value of 321 GPa for AlN matches values given in the literature. Virtually no increase in Young's modulus with increasing SiC whisker content was observed, despite a modulus of 500-700 GPa for SiC whiskers. For both 10 vol% and 20 vol% SiC whisker samples a value of 326 GPa was measured. Using data from Ruh *et al.* [2.3-6], a zero porosity correction for Young's modulus, based

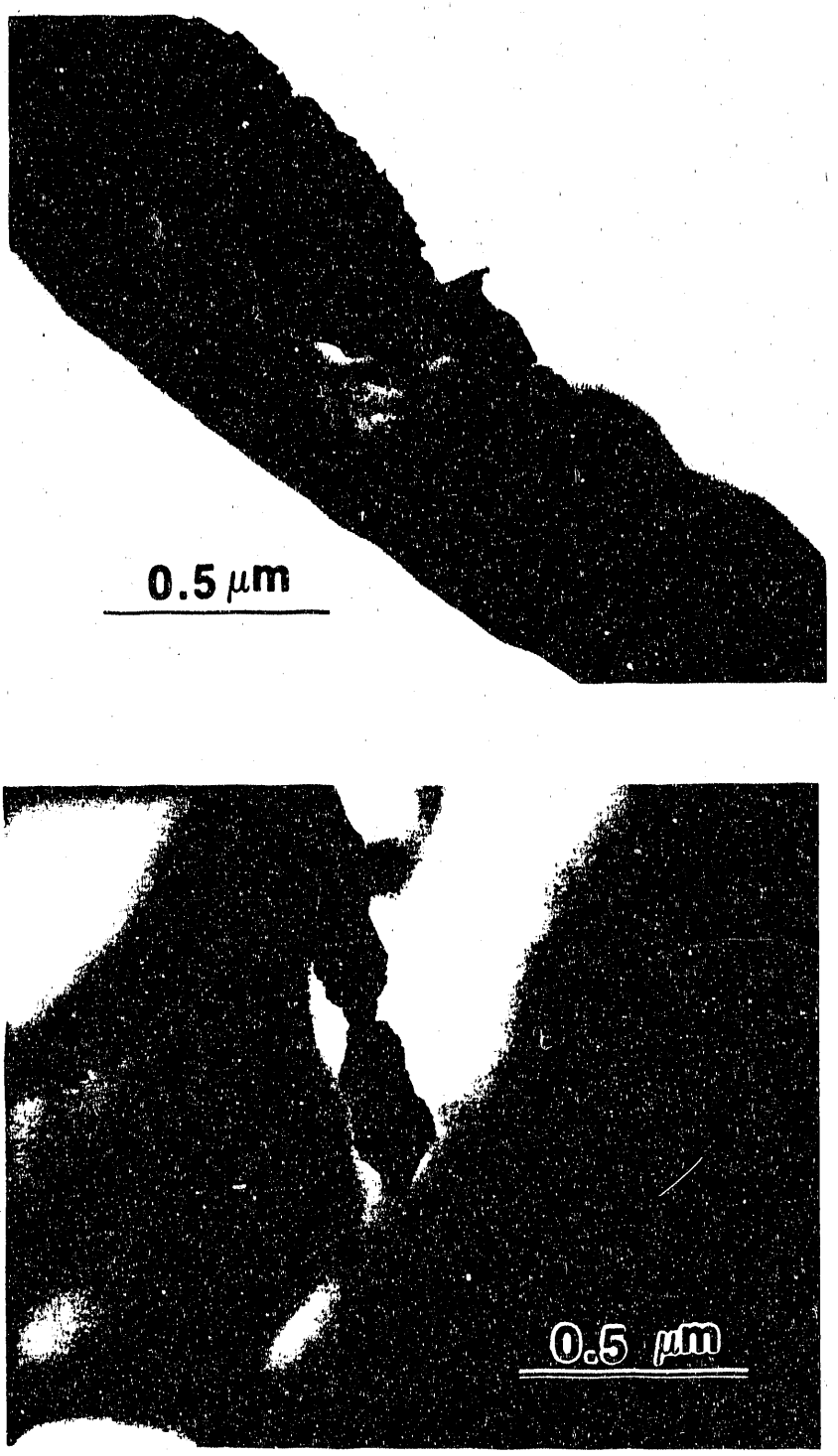

Figure 28. SiC whiskers Embedded within AlN Grains Show Irregular Morphologies, Suggesting Solid Solution Formation. (A3Y10W Composites $PL_{(PB=AlN)}$ 1800°C, 0.5 hr.

Table 11. Elastic Moduli of AlN-SiCw Composites.

Composition	Hot-Pressing Conditions	Measured Density (g/cm^3)	Percent of Corrected Theoretical Density	Shear Modulus (GPa)	Poisson's Ratio	Measured Modulus (GPa)	Calculated Modulus (GPa) Ref. [47]	Zero Porosity Modulus (GPa)
A3Y	HP 1600°C, 1 hr, vac	3.37	99.7	129	0.23	316	321	318
	HP 1800°C, 0.5 hr, 0.5 atm Ar	3.39	~ 100	131	0.23	321	322	321
A0Y10W	HP 1700°C, 1 hr, vac	3.15	96.1	103	0.21	249	293	268
	HP 1800°C, 0.5 hr, 0.5 atm Ar	3.24	98.8	121	0.22	294	313	297
A3Y10W	HP 1600°C, 1 hr, vac	3.11	92.5	84	0.19	200	268	233
	HP 1700°C, 1 hr, vac	3.40	~ 100	141	0.23	346	322	347
	HP 1800°C, 0.5 hr, 0.5 atm Ar	3.32	98.7	133	0.23	327	312	337
A3Y20W	HP 1800°C, 0.5 hr, 0.5 atm Ar	3.29	98.0	134	0.22	327	307	341

on AlN, was made and is shown in Figure 29. Limits given by the rule of mixtures (ROM) are also shown.

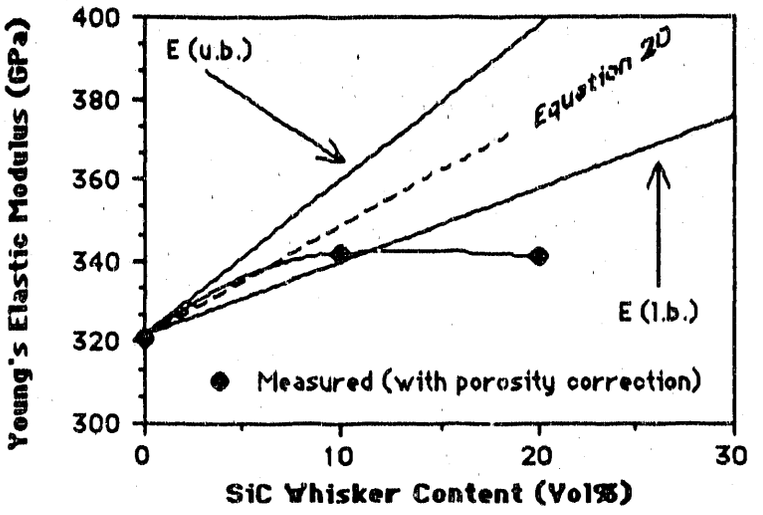

Figure 29. Young's Modulus as a Function of SiC Whisker Content. [Assuming $E_{whisker}$ (E_w) = 700 GPa, $E_{AlN\ matrix}$ (E_m) = 322 GPa]

The elastic modulus of composites can be estimated by a rule of mixtures (ROM). An upper bound [E(u.b.)] ROM exists based on two phases being parallel to the test direction (iso-strain condition), while a lower bound [E(l.b.)] ROM is based on two phases being perpendicular to the test direction (iso-stress condition). Equations 18 and 19 show the relationships for the two cases, respectively [89].

$$E_{\parallel} = E_1V_1 + E_2V_2 \qquad \{18\}$$

$$E_{\perp} = (E_1E_2)/(E_2V_1 + E_1V_2) \qquad \{19\}$$

where E_1, V_1, E_2, and V_2 are the Young's elastic modulus and volume fraction of phases 1 and 2, respectively.

If the phases are not unidirectionally oriented but are randomly oriented in planes, the composite modulus (E) can be simply estimated from the above two cases as [89].

$$E = 3/8\ E_{\parallel} + 5/8\ E_{\perp} \qquad \{20\}$$

The spread in the two limits depends on the value assumed for the modulus of the SiC whiskers. The modulus for the SiC whiskers (E_w) was assumed to lie between 500 and 700 GPa (700 GPa assumed here), while the modulus of the AlN matrix (E_m) used was 322 GPa. The zero porosity corrected composite data has a better fit with the lower bound (Equation 19). This can be explained by the fact that the Young's modulus was tested parallel to the hot-pressing direction and considering the tendency for whiskers to slightly align perpendicular to the hot-pressing direction.

The discrepancy between the data and the above equations (particularly for the 20 vol% SiC whisker sample, which had a modulus below the lower bound) is most likely associated with porosity not accounted for in the zero porosity correction. The zero porosity correction was based only on AlN and, therefore, should account for matrix porosity in the composites. However, some porosity was observed in composites near SiC whiskers at grain boundaries, and between whiskers that were not homogeneously dispersed but agglomerated together. This porosity, which affects load transfer and perhaps makes the iso-strain assumption invalid (and therefore, the $E_{\parallel}$ value invalid) is not accounted for in the matrix correction. A non-homogeneous distribution of whiskers would also differ from the ROM calculation based on a homogeneous distribution of phases. The data also does not seem to match the equation based on an in-plane random

orientation well (Equation 20). The measured value for the 20 vol% SiC whisker composite also falls below the value predicted by this equation. Since Equation 20 is based on $E_{\parallel}$ and $E_{\perp}$, it is not surprising that it also does not fit the data even though the SiC whiskers tend to have in-plane random orientation after hot-pressing.

2. Fracture Toughness

The indentation fracture toughness as a function of SiC whisker content is shown in Figure 30. Crack length data for indentation loads of 7 and 8 kg (68.6 and 78.4 N) were averaged together. Two equations were used to calculate K_{IC} in $Pa \cdot m^{1/2}$. Equation 4 was proposed by Lawn and Fuller [65], and Equation 5 was proposed by Anstis *et al.* [67].

$$K_{IC} = [1/(\pi^{3/2} \tan 68°)]P/c^{3/2} \quad \{4\}$$

$$K_{IC} = 0.016(E/H)^{1/2} P/c^{3/2} \quad \{5\}$$

where P is the indentation load (N), c is the crack length (m), and E is Young's modulus (GPa), and H is the hardness (GPa). The Lawn and Fuller equation better matches the literature K_{IC} values for AlN of ≈ 2.7 $MPa \cdot m^{1/2}$ measured in three point bend [1, 2]. Both equations show a higher value for AlN than a value of 1.8 $MPa \cdot m^{1/2}$, reported by Witek *et al.*, [3] measured by indentation for AlN sintered with 2 wt% CaO at a load of 98 N.

The Lawn and Fuller relation shows a steadily increasing fracture toughness with SiC whisker content with a maximum increase of ≈ 33%. The Anstis *et al.* relation shows a maximum increase in fracture toughness of ≈ 18%, with only a very slight increase between the 10 and 20 vol% SiC whisker composites. By including the material

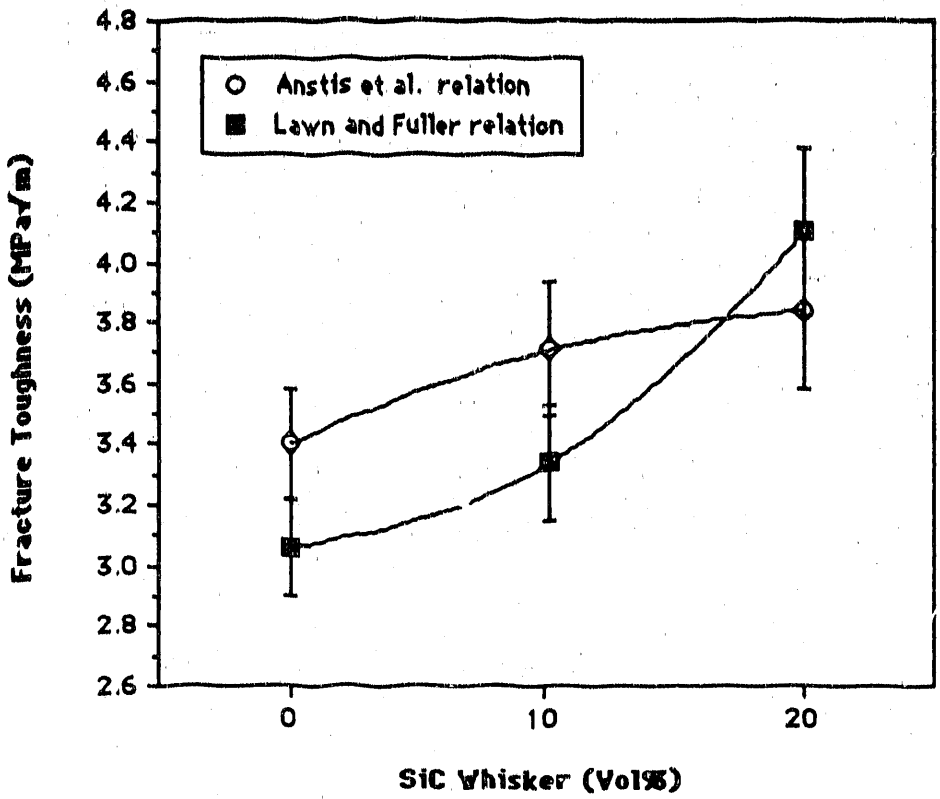

Figure 30. Indentation Fracture Toughness
As a Function of SiC whisker Content.

parameters E and H in the calculation of the fracture toughness, it appears that the Anstis relation may be more sensitive to the sample microstructure, particularly the density; the increase in the fracture toughness of the 20 vol% SiC whisker samples is nearly offset by its lower density. Another reason for different values from the two equations may be the introduction of error in determining the E/H ratio by Knoop indentation. This ratio is only used in the Anstis equation.

The moderate increase in the fracture toughness indicates the potential for toughening in the AlN-SiC whisker system. These composites could be considered as engineering materials, but with an

emphasis on applications where a high thermal conductivity and/or high electrical resistivity material is needed.

E. Operative Toughening Mechanisms

Indented samples were viewed in the SEM to observe the Vickers crack-microstructure interaction and assess the operative toughening mechanisms. Because the thermal expansion of the SiC whiskers is less than AlN, (α_{SiC} = 4.5 x 10^{-6}/°C, α_{AlN} = 5.6 x 10^{-6}/°C) hoop tension and radial compression in the AlN matrix and compression in the SiC whiskers are expected. In this case the crack is attracted to the whisker. Figure 31 shows that the cracks are attracted to the whisker and impeded until fracture of the whisker occurs.

In many instances, strong bonding between matrix and whisker is seen, as in Figure 32. Strong bonding suggests some strengthening, and hence toughening, can occur by load transfer to the stronger whiskers since $E_w/E_m \approx 2$ [83] assuming E_w = 700 GPa and E_m = 322 GPa. Assuming that the whiskers are oriented randomly in planes perpendicular to the hot-pressing direction, the strength increment (and toughening contribution) can be estimated from Equation {11}:

$$\sigma_o' = \sigma_{mu} \{1 + (V_f/3) [(E_f/E_m) - 1]\} \quad \{11\}$$

where σ_o' is the stress at which microcracks appear, σ_{mu} is the matrix stress at its breaking strain, E_f and E_m the elastic modulus of the fiber and matrix, respectively and V_f is the volume fraction of the fibers (whiskers). Assuming $E_f/E_m = E_w/E_m = 2$ for and $V_f = 0.20$, $\sigma_o' \approx 1.07$ σ_{mu} or an increase in strength of ≈ 7%.

Bridging mechanisms also contribute to the increased toughness of the composites. Figure 33 shows crack bridging by intact grains

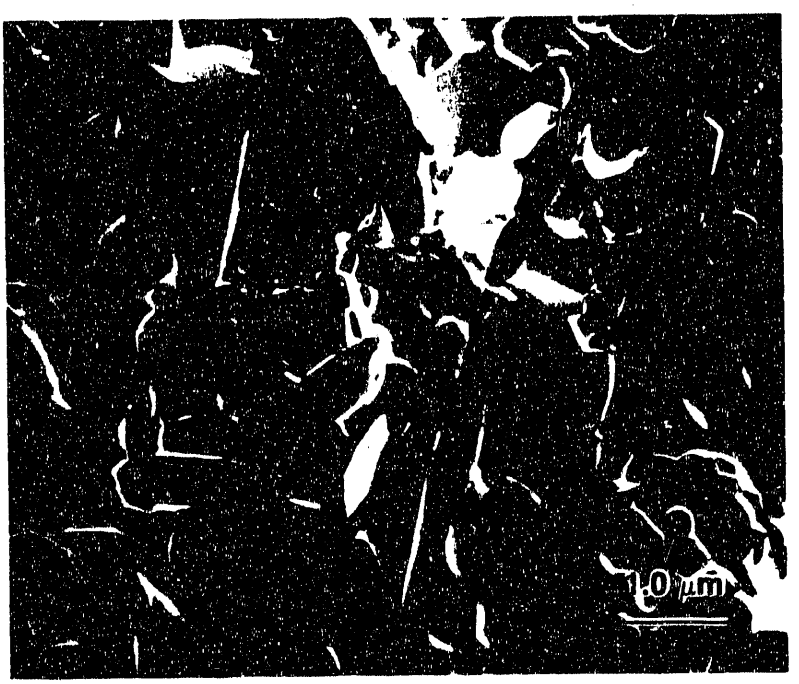

Figure 31. SEM Micrograph Showing Cracking Around Whiskers in A3Y20W HP 1800°C, 0.5 hr Composites.

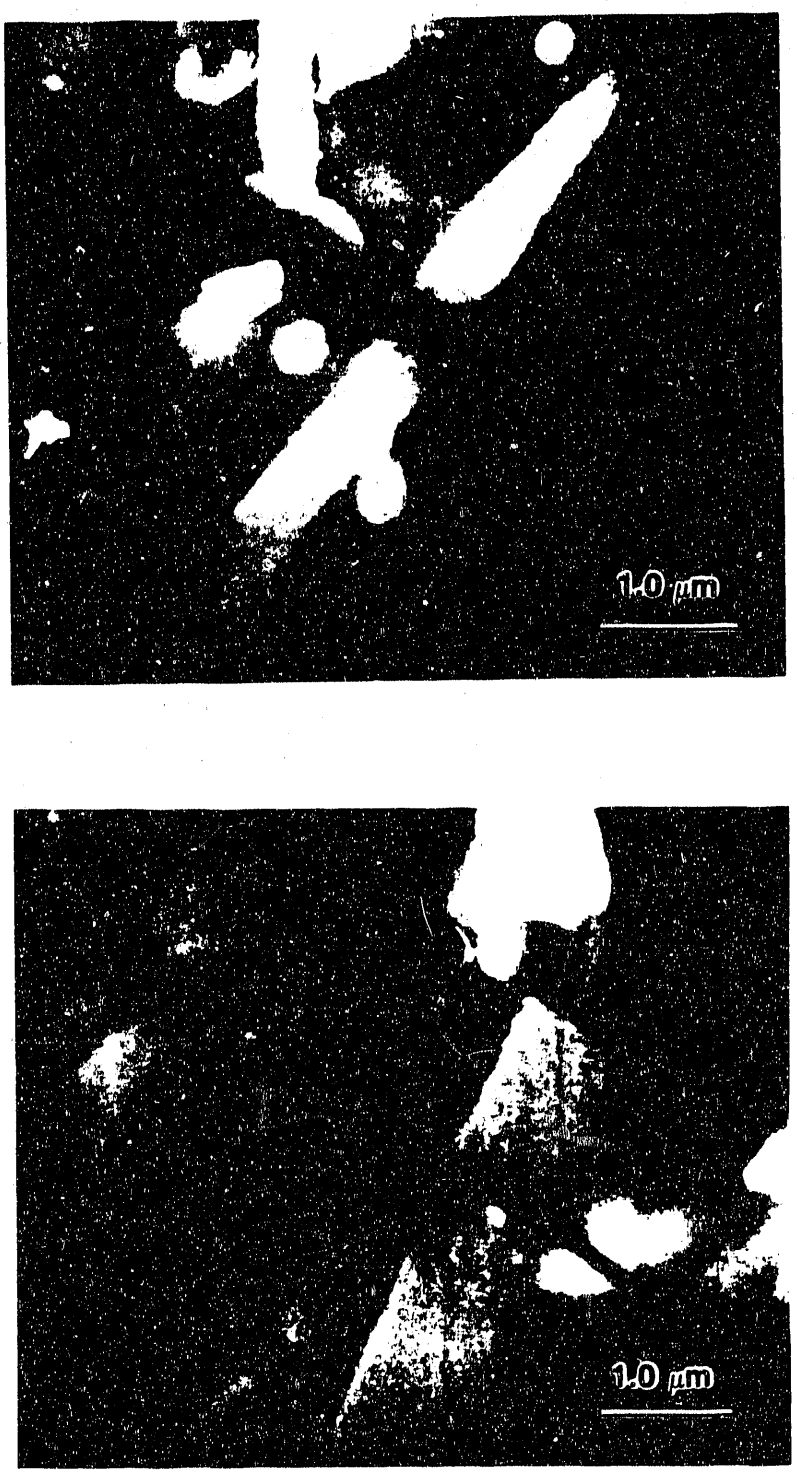

Figure 32. Strong Bonding Between Matrix and Whiskers in A3Y20W Composites HP at 1800°C, 0.5 hr.

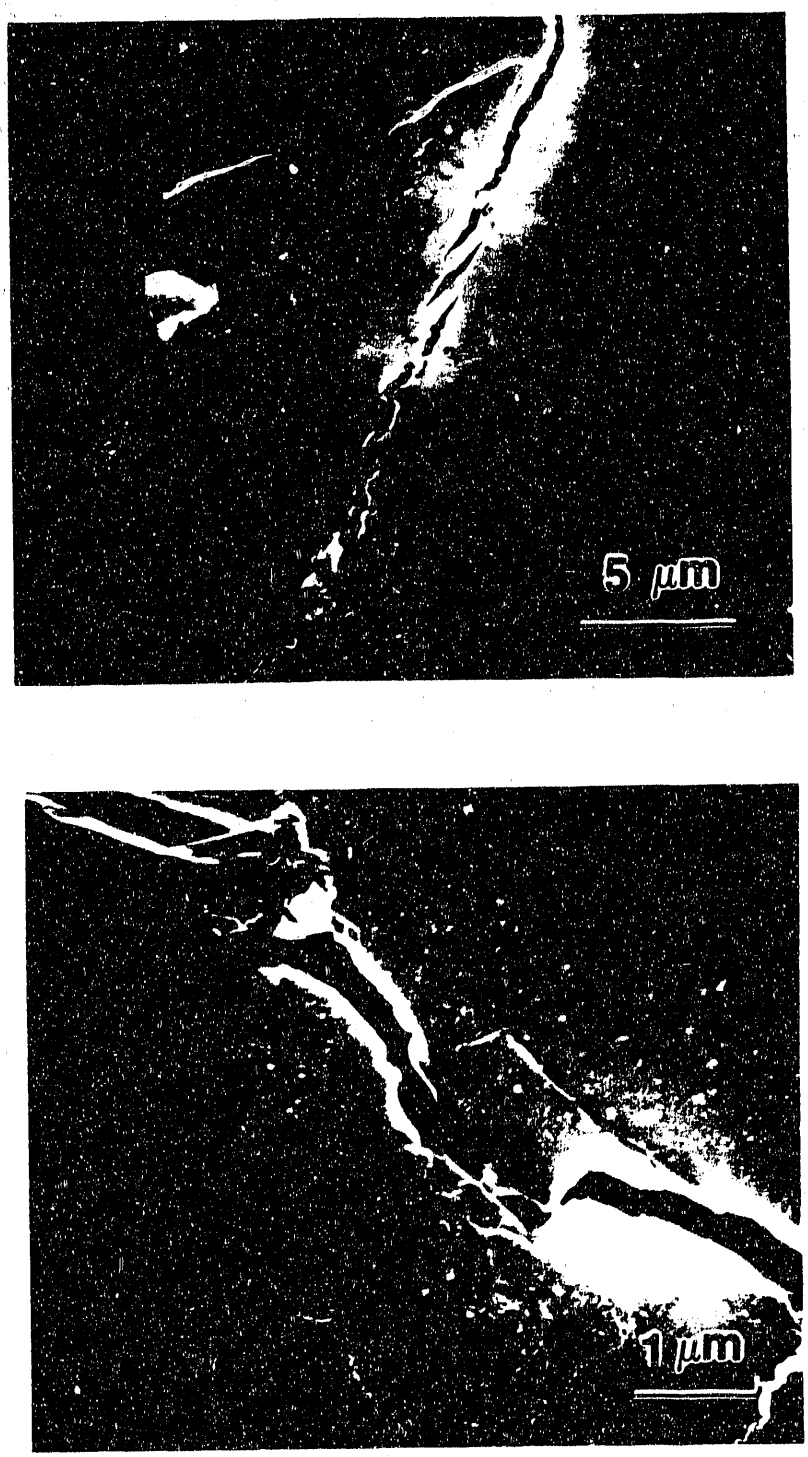

Figure 33. Crack Bridging by Grains in A3Y HP 1600°C, 1 hr.

operates in unreinforced AlN. Some grain bridging was also observed within the matrix of the composites. Crack bridging by whiskers is shown in Figure 34. A maximum debond length of ≈ 2R was observed, where R is the whisker radius. This compares to debond values of between 2R and 6R in Al_2O_3-SiC whisker composites and between R and 3R in Si_3N_4-SiC whisker composites [73]. In Al_2O_3-SiC whisker composites, the interface is under residual compression, while the interface in Si_3N_4-SiC whisker composites is under residual tension. Interfaces in AlN-SiC whisker should also be under residual compression (due to thermal expansion mismatches) but the observed debond length is much less than that in Al_2O_3-SiC whisker composites.

Campbell *et al.* [73] point out that since residual strain is invariably detrimental to debonding and bridging, matched thermal expansions (between matrix and whisker) are desirable. In this regard, the closer match of thermal expansions between AlN and SiC than Al_2O_3 ($\alpha = 7.5 \times 10^{-6}/°C$) and SiC should enhance debonding and bridging. However, the limited debond length indicates that the interface is relatively strong, which suggests that some solid solution between the SiC whisker and AlN has occurred even in the hot-pressed samples.

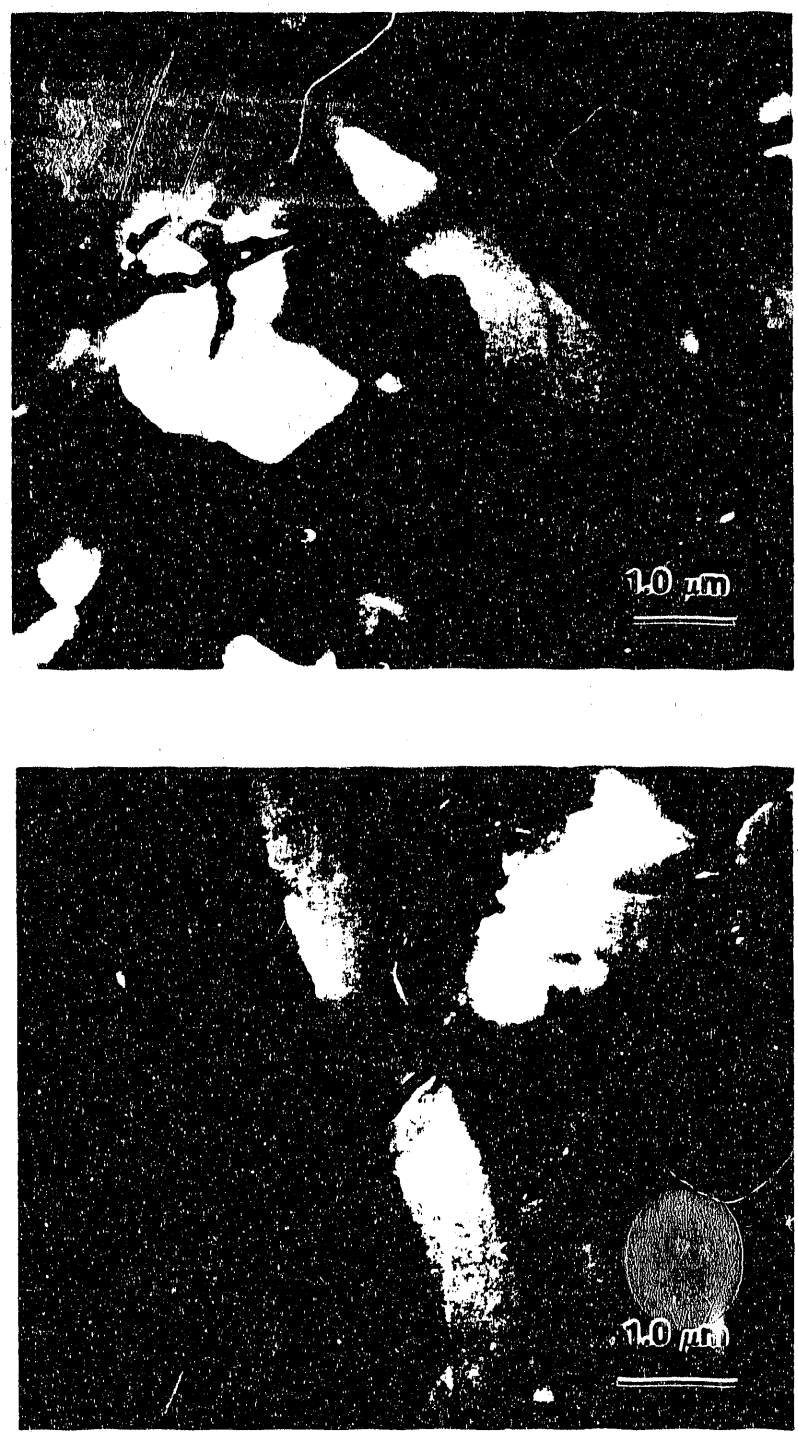

Figure 34. Crack Bridging by Whiskers in A3Y20W Composites. A Maximum Debond Length of ≈ 2R is Observed (R = Whiskers Radius).

V. SUMMARY

1. Aluminum nitride + 3 wt% Y_2O_3 (A3Y) can be hot-pressed to full density at 1600°C. Pressureless sintering at 1750°-1800°C resulted in densities of 95-97%.

2. Aluminum nitride + 3 wt% Y_2O_3 + 10 vol% SiC whiskers (A3Y10W) composites hot-pressed at 1700°C and 1800°C to densities >98% and sintered to densities of 93-95% at 1800°C. Aluminum nitride + 10 vol% SiC whiskers (A0Y10W) showed densities of 96% and 99% when hot-pressed at 1700°C and 1800°C, respectively.

3. Aluminum nitride + 3 wt% Y_2O_3 + 20 vol% SiC whiskers (A3Y20W) composites hot-pressed to a density of 98% at 1800°C, but sintering densities did not exceed 70%.

4. The type of protective powder bed used during sintering affected the amount of oxygen within the samples. A high oxygen content was measured in samples sintered in an AlN powder bed or without a powder bed. A low oxygen content was found in samples sintered in a SiC + 20 vol% C powder bed. No oxygen was detected in hot-pressed samples.

5. Degradation of SiC whiskers was observed in high oxygen containing samples, but not in low oxygen content samples. This degradation was manifest as reaction products from the reaction of SiC whiskers and sintering additives.

6. Measurements of SiC diffusion in AlN and HREM observations gave evidence of SiC-AlN solid solution formation in pressureless sintered low oxygen content samples. SiC could be measured in AlN at distances > 1μm from the whisker. No SiC diffusion in AlN was measured at distance as small as ≈ 0.2 μm. Diffusion of SiC in AlN could not be measured in high oxygen content samples due to a high background level of Si.

7. Young's modulus showed only a slight increase from 322 GPa for AlN to 341 for the 20 vol% SiC whisker composite. Values were somewhat below those predicted by composite theory.

8. Fracture toughness measurements by the indentation technique showed a 33% increase in K_{IC} when calculated using the Lawn and Fuller equation and 18% increase in K_{IC} when calculated using the equation proposed by Anstis *et al.*

9. Operative toughening mechanisms include crack deflection and crack bridging. A maximum debond length of one whisker diameter was observed is HP composites. A contribution of ≈ 7% to the toughness due to load transfer was estimated.

10. The moderate increase in the fracture toughness indicates the potential for toughening in the AlN-SiC whisker system. The limited toughness in AlN-SiC whisker composites is a consequence of whisker degradation. Reducing the oxygen impurity within the composites has been shown to be successful

in reducing whisker degradation by eliminating the reaction between the SiC whiskers and the sintering additives. However, it appears that the formation of SiC-AlN solid solution cannot be avoided, and results in a moderate toughness increase due to strong bonding between the matrix and whisker. Therefore, it would appear that AlN-SiC whisker composites might only be considered in engineering applications where a material with high thermal conductivity and/or high electrical resistivity is needed.

VI. REFERENCES

1. P. Boch, J. C. Glandus, J. Jarrige, J. P. Lecompte, and J. Mexmain, "Sintering, Oxidation and Mechanical Properties of Hot Pressed Aluminum Nitride," *Ceram. Int.*, **8** [1] 34-40 (1982).

2. G. DeWith and N. Hattu, "High-Temperature Fracture of Hot-Pressed AlN Ceramics," *J. Mater. Sci.*, **18** 503-07 (1983).

3. S. R. Witek, G. A. Miller, and M. P. Hamer, "Effects of CaO of the Strength and Toughness of AlN," *J. Am. Ceram. Soc.*, **72** [3] 469-73 (1989).

4. P. F. Becher and G. C. Wei, "Toughening Behavior in SiC-Whisker-Reinforced Alumina," *J. Am. Ceram. Soc.*, **64** [12] C-267-C-269 (1984).

5. G. C. Wei and P. F. Becher, "Development of SiC-Whisker-Reinforced Ceramics," *Am. Ceram. Soc. Bull.*, **64** [2] 298-304 (1985).

6. A. H. Chokshi and J. R. Porter, "Creep Deformation of an Alumina Matrix Composite Reinforced with Silicon Carbide Whiskers," *J. Am. Ceram. Soc.*, **68** [6] C-144-C-145 (1985).

7. J. Homeny, W. L. Vaughn, and M. K. Ferber, "Processing and Mechanical Properties of SiC-Whisker-Al_2O_3-Matrix Composites, *Am. Ceram. Soc. Bull.*, **66** [2] 333-38 (1987).

8. J. R. Porter, F. F. Lange, and A. H. Chokshi, "Processing and Creep Performance of SiC-Whisker-Reinforced Al_2O_3," *Am. Ceram. Soc. Bull.*, **66** [2] 343-47 (1987).

9. T. N. Tiegs and P. F. Becher, "Sintered Al_2O_3-SiC-Whisker Composites," *Am. Ceram. Soc. Bull.*, **66** [2] 339-42 (1987).

10. S. Yamada, "Recent Research on SiC Whisker-Reinforced Ceramic Composites in Japan," *ONRFE Sci. Bul.* **12** [4] 17-44 (1987).

11. P. F. Becher and T. N. Tiegs, "Temperature Dependence of Strengthening by Whisker Reinforcement: SiC Whisker-Reinforcement of Alumina in Air," *Adv. Ceram. Mat.*, **3** [12] 148-53 (1988).

12. L. Bjork and L. A. G. Hermansson, "Hot Isostatically Pressed Alumina-Silicon Carbide-Whisker Composites," *J. Am. Ceram. Soc.*, **72** [8] 1436-38 (1989).

13. S. Iio, M. Watanabe, M. Matsubara, and Y. Matsuo, "Mechanical Properties of Alumina/Silicon Carbide Whisker Composites," *J. Am. Ceram. Soc.*, **72** [10] 1880-84 (1989).

14. T. N. Tiegs and P. F. Becher, "Whisker-Reinforced Ceramic Composites"; pp. 639-45 in Tailoring Multiphase and Composite Ceramics. Edited by R. E. Tressler, G. L. Messing, C. G. Pantano, and R. E. Newnham. Plenum Press, New York, 1986.

15. M. I. Osendi, B. A. Bender, and D. Lewis III, "Microstructure and Mechanical Properties of Mullite-Silicon Carbide Composites," *J. Am. Ceram. Soc.*, **72** [6] 1049-54 (1989).

16. R. Hayami, K. Veno, I. Kondou, N. Tamari, and Y Toibana, "Si_3N_4-SiC Whisker Composite Material"; pp. 663-74 in Tailoring Multiphase and Composite Ceramics. Edited by R. E. Tressler, G. L. Messing, C. G. Pantano, and R. E. Newnham. Plenum Press, New York, 1986.

17. P. D. Shalek, J. J. Petrovic, G. F. Hurley, and F. D. Gac, "Hot-Pressed SiC Whisker/Si_3N_4 Matrix Composites," *Am. Ceram. Soc. Bull.*, **65** [2] 351-56 (1986).

18. S. T. Buljan, J. G. Baldoni, and M. L. Huckabee, "Si_3N_4-SiC Composites," *Am. Ceram. Soc. Bull.*, **66** [2] 347-52 (1987).

19. R. Lundberg, L. Kahlman, R. Pompe, R. Carlsson, and R. Warren, "SiC-Whisker Reinforced Si_3N_4 Composites," *Am. Ceram. Soc. Bull.*, **66** [2] 330-33 (1987).

20. G. Pezzotti, I. Tanaka, T. Okamoto, M. Koizumi, and Y. Miyamoto, "Processing and Mechanical Properties of Dense Si_3N_4-SiC Whisker Composites without Sintering Aids," *J. Am. Ceram. Soc.*, **72** [8] 1461-64 (1989).

21. H. Kodama, T. Suzuki, H. Sakamoto, and T. Miyoshi, "Toughening of Silicon Nitride Matrix Composites by the Addition of Both Silicon Carbide Whiskers and Silicon Carbide Particles," . *Am. Ceram. Soc.*, **73** [3] 678-83 (1990).

22. G. A. Slack, "Nonmetallic Crystals with High Thermal Conductivity," *J. Phys. Chem. Solids*, **34**, 321-35 (1973).

23. N. Kuramoto, H. Taniguchi, and I. Aso, "Translucent AlN Ceramic Substrate," *IEEE Trans. Compon., Hybrids, Manuf. Technol.*, **CHMT-9** [4] 386-90 (1986).

24. R. A. Youngman and D. A. Chernoff, "Cathodoluminescence in Aluminum Nitride," *Am. Ceram. Soc. Bull.*, **66** [8] 1233 (1987).

25. G. A. Slack, R. A. Tanzilli, R. O. Pohl, and J. W. VanderSande, "The Intrinsic Thermal Conductivity of AlN," *J. Phys. Chem. Solids*, **48** [7] 641-47 (1987).

26. S. Prochzka and C. F. Bobik, "Sintering of Aluminum Nitride"; pp. 321-32 in Materials Science Research, Vol. 13. Edited by G. C. Kuczyski. Plenum Press, New York and London, 1979.

27. Y. Kurokawa, K. Utsumi, and H. Takamizawa, "Development and Microstructural Characterization of High-Thermal-Conductivity Aluminum Nitride Ceramics," *J. Am. Ceram. Soc.*, **71** [7] 588-94 (1988).

28. I. C. Huseby and R. F. Bobik, "High Thermal Conductivity Aluminum Nitride Ceramic Body," U. S. Pat. No. 4 547 471, Oct. 15, 1985.

29. I. C. Huseby and R. F. Bobik, "Pressureless Sintering Process to Produce High Thermal Conductivity Ceramic Body of Aluminum Nitride," U. S. Pat. Nos. 4 578 232 - 4 578 234, Mar. 25, 1986.

30. I. C. Huseby and R. F. Bobik, "High Thermal Conductivity Ceramic Body of Aluminum Nitride," U. S. Pat. Nos. 4 578 384 and 4 578 365, Mar. 25, 1986.

31. A. V. Virkar, T. B. Jackson, and R. A. Cutler, "Thermodynamic and Kinetic Effects of Oxygen Removal on the Thermal Conductivity of Aluminum Nitride," *J. Am. Ceram. Soc.*, **72** [11] 2031-42 (1989).

32. N. Kuramoto, H. Taniguchi, and I. Aso, "Development of Translucent Aluminum Nitride Ceramics," *Am. Ceram. Soc. Bull.*, **68** [4] 883-87 (1989).

33. T. Sakai and M. Iwata, "Effect of Oxygen on Sintering of AlN," *J. Mater. Sci.*, **12** 1659-65 (1977).

34. D. Fister, "AlN and BN Powders for Advanced Applications," *Ceram. Eng. Sci. Proc.* **6** [9-10] 1305-09 (1985).

35. K. A. Schwetz, H. Knoch, and A. Lipp, "Sintering of Aluminum Nitride with Low Oxide Addition"; pp. 245-252 in Progress in Nitrogen Ceramics. Edited by Riley. Nato ASI, Series E **65**, Martinus Nijhoff, Boston, 1983.

36. T. B. Troczynski and P. S. Nicholson, "Effect of Additive on the Pressureless Sintering of Aluminum Nitride between 1500°C and 1800°C," *J. Am. Ceram. Soc.*, **72** [8] 1488-91 (1989).

37. N. S. VanDamme, S. M. Richard, and S. R. Winzer, "Liquid-Phase Sintering of Aluminum Nitride by Europium Oxide Additive," *J. Am. Ceram. Soc.*, **72** [8] 1409-14 (1989).

38. K. Anzai, N. Iwase, K. Shinozaki, and T. Akihiko, "Development of High Thermal Conductive Aluminum Nitride Substrate Materials by Pressureless Sintering," *Toshiba Review*, 23-8 (1987).

39. Figure 2344 in Phase Diagrams for Ceramists 1969 Supplement. Edited by M. K. Reser. The American Ceramic Society, Columbus, 1969.

40. J. W. McCauley and N. D. Corbin, " High Temperature Reactions and Microstructures in the Al_2O_3-AlN-System"; pp. 111-18 in Progress in Nitrogen Ceramics. Edited by F. L. Riley. Martinus Nijhoff, Boston, 1983.

41. U. Topfer and G. Muller, "Pressure sintering of AlN with Y-containing Additives," *CFI, Ceram. Forum. Int.*, **65** [2] 70-74 (1988).

42. K. Komeya and M. Inoue, "Sintering of Aluminum Nitride: Particle Size Dependence of Sintering Kinetics," *J. Mater. Sci.*, **4** 1045-5-(1969).

43. G. A. Jeffrey, G. S. Parry, and L. Mozzir, "Study of the Wurtzite-type Binary Compounds: I, Structures of AlN and BN," *J. Chem. Phys.*, **25** 1024 (1956).

44. G. Long and L. M. Foster, "Aluminium Nitride, A Refractory for Aluminum to 2000°C," *J. Am. Ceram. Soc.*, **42** [2] 53-9 (1959).

45. M. Billy and J. Mexmain," Processing and Properties of Aluminum Nitride, a New Candidate for High Temperature Applications," *Sprechsaal*, **118** [3] 245-49 (1985).

46. J. C. Glandus, J. L. Besson, and P. Boch, "High Temperature Properties of Some Nitrogen Ceramics"; pp. 419-24 in Science of Ceramics, Vol. 11, 1981.

47. R. Ruh, A. Zangvil, and J. Barlowe, "Elastic Properties of SiC, AlN, and their Solid Solutions and Particulate Composites," *Am. Ceram. Soc. Bull.*, **64** [10] 1368-74 (1985).

48. D. Gerlich, S. L. Dole, and G. A. Slack, "Elastic Properties of Aluminum Nitride," *J. Phys. Chem. Solids*, **47** [5] 437-41 (1986).

49. R. Ruh and A. Zangvil, "Composition and Properties of Hot-Pressed SiC-AlN Solid Solutions," *J. Am. Ceram. Soc.*, **65** [5] 260-65 (1982).

50. K. Komeya and F. Noda, "Aluminum Nitride and Silicon Nitride for High Temperature Gas Turbine Engines," Automotive Engineering Congress, Detroit MI, Feb 25- March 1 (1974).

51. A. Zangvil and R. Ruh, "Alloying of Silicon Carbide with Other Ceramic Compounds - A Review"; pp. 63-82 in Ceramic Transactions, Silicon Carbide '87, Vol. 2. Edited by J. D. Cawley and C. E. Semler. The American Ceramic Society, Inc., Westerville, OH,1989.

52. P. T. B. Schaffer, "Review of The Structure of Silicon Carbide," *Acta Crystallogr., Sect. B*, **25** [Pt3] 477-88 (1969).

53. Z. Li and R. C. Bradt, "Thermal Expansion and Thermal Expansion Anisotropy of SiC Polytypes," *J. Am. Ceram. Soc.*, **70** [7] 445-48 (1987).

54. C. H. McMurtry, W. D. G. Boecker, S. G. Seshadri, J. S. Zanghi, and J. E. Garnier, "Microstructure and Material Properties of SiC-TiB_2 Particulate Composites," *Am. Ceram. Soc. Bull.*, **66** [2] 325-29 (1987).

55. A. Zangvil and R. Ruh, "Phase Relationships in the Silicon Carbide-Aluminum Nitride System," *J. Am. Ceram. Soc.*, **71** [10] 884-90 (1988).

56. W. Ranfaniello, K. Cho, and A. V. Virkar, "Fabrication and Characterization of SiC-AlN Alloys," *J. Mater. Sci.*, **16** [12] 349-88 (1981).

57. A. Zangvil and R. Ruh, "Solid Solutions and Composites in the SiC-AlN and SiC-BN Systems," *Materials Science and Engineering*, **71** 159-64 (1985).

58. J. V. Milewski, F. D. Gac, J. J. Petrovic, and S. R. Skaggs, "Growth of Beta-Silicon Carbide Whiskers by the VLS Process," *J. Mater. Sci.*, **20**, 1160-66 (1985).

59. J. Lee and I. B. Cutler, "Formation of Silicon Carbide from Rice Hulls," *Am. Ceram. Soc. Bull.*, **54** [2] 195-98 (1975).

60. S. R. Nutt, "Defects in Silicon Carbide Whiskers," *J. Am. Ceram. Soc.*, **67** [6] 428-31 (1984).

61. J. J. Petrovic, J. V. Milewski, D. L. Rohr, and F. D. Gac, "Tensile Mechanical Properties of SiC Whiskers," *J. Mater. Sci.*, **20** 1167-77 (1985).

62. K. P. Gadkaree and K. Chyung, "Silicon Carbide Whisker-Reinforced Glass and Glass-Ceramic Composites," *Am. Ceram. Soc. Bull.*, **65** [2] 370-76 (1986).

63. A. G. Evans and E. A. Charles, "Fracture Toughness Determinations by Indentation," *J. Am. Ceram. Soc.*, **59** [7-8] 371-72 (1976).

64. A. G. Evans; pp. 112-35 in Fracture Mechanics Applied to Brittle Materials. ASTM STP 678. Edited by S. W. Freiman. American Society for Testing and Materials, Philadelphia, PA, 1979.

65. B. R. Lawn and E. R. Fuller, "Equilibrium Penny-Like Cracks in Indentation Fracture," *J. Mater. Sci.*, **10** 2016-24 (1975).

66. B. R. Lawn, A. G. Evans, and D. B. Marshall, "Elastic/Plastic Indentation Damage in Ceramics: The Median/Radial Crack System" *J. Am. Ceram. Soc.*, **63** [9-10] 574-81 (1980).

67. G. R. Anstis, P. Chantikul, B. R. Lawn, and D. B. Marshall, "A Critical Evaluation of Indentation Techniques for Measuring Fracture Toughness: I, Direct Crack Measurements," *J. Am. Ceram. Soc.*, **64** [9] 533-38 (1981).

68. D. B. Marshall, T. Noma, and A. G. Evans, "A Simple Method for Determining Elastic-Modulus-to-Hardness Ratios using Knoop Indentation Measurements," *J Am. Ceram. Soc.*, **65** [10] C-175-C-176 (1982).

69. K. Breder, K. Zeng, and D. J. Rowcliffe, "Indentation Testing of an Al_2O_3/SiC Whisker Composite," *Ceram. Eng. Sci. Proc.*, **10** [7-8] 1005-13 (1989).

70. M. Ruhle, B. J. Dagleish, and A. G. Evans, "On the Toughening of Ceramics by Whiskers," *Scr. Metall.*, **21** [5] 681-86 (1987).

71. P. Becher, C. H. Hsueh, P. Angelini, and T. N. Tiegs, "Analysis of Toughening in Whisker Reinforced Ceramics," *Mater. Sci. Eng.*, **A107**, 257-61 (1989).

72. K. T. Faber and A. G. Evans, "Crack Deflection Processes: I. Theory," *Acta Metall.*, **31** [4] 565-76 (1983).

73. G. H. Campbell, M. Ruhle, B. J. Dagleish, and A. G. Evans, "Whisker Toughening: A Comparison Between Aluminum Oxide and Silicon Nitride Toughened with Silicon Carbide," *J. Am. Ceram. Soc.*, **73** [3] 521-30 (1990).

74. K. T. Faber and A. G. Evans, "Crack Deflection Processes: II. Experiment," *Acta Metall.*, **31** [4] 577-84 (1983).

75. K. T. Faber and A. G. Evans, "Intergranular Crack-Deflection Toughening in Silicon Carbide," *J. Am. Ceram. Soc.*, **66** [6] C-94-C-96 (1983).

76. M. Y. He and J. W. Hutchinson, "Kinking of a Crack Out of an Interface," *J. Appl. Mech.*, **111** (*Trans. ASME*, **56** [2]) 270-78 (1989).

77. D. B. Marshall and A. G. Evans, "The Influence of Residual Stress on the Toughness of Reinforced Brittle Materials," *Mater. Forum*, **11**, 304-12 (1988).

78. P. G. Charalambides and A. G. Evans, "Debonding Properties of Residually Stressed Brittle Matrix Composites," *J. Am. Ceram. Soc.*, **72** [5] 746-53 (1989).

79. L. S. Sigl and A. G. Evans, "Effects of Residual Stress on Pull-Out in Brittle Matrix Composites," *Mech. Mater.*, **8**, 1-12 (1989).

80. R. F. Cook, B. R. Lawn, and C. J. Fairbanks, "Microstructure-Strength Properties in Ceramics: I, Effect of Crack Size on Toughness," *J. Am. Ceram. Soc.*, **68** [11] 604-15 (1985).

81. B. R. Lawn, "Physics of Fracture," *J. Am. Ceram. Soc.*, **66** [2] 83-91 (1983).

82. A. G. Evans, "Perspective on the Development of High-Toughness Ceramics," *J. Am. Ceram. Soc.*, **73** [2] 187-206 (1990).

83. R. W. Rice, "Mechanisms of Toughening in Ceramic Matrix Composites," *Ceram. Eng. Sci. Proc.*, **2** [7-8] 661-701 (1981).

84. K. K. Chawla in Composite Materials Science and Engineering. Springer-Verlag, New York, 1987.

85. A. Kelly and G. J. Davies, "The Principles of the Fibre Reinforcement of Metals," *Metallurgical Reviews*, **10** [37] 1-77 (1965).

86. H. L. Cox, "The Elasticity and Strength of Paper and Other Fibrous Materials," *Brit. J. of Appl. Physics*, **3** 72-9 (1952).

87. J. Rhodes, Advanced Composite Materials Corporation. Private communication.

88. E. Schreiber, O. L. Anderson, and N. Soga, Elastic Constants and Their Measurement. McGraw Hill, New York, 1974.

89. D. Hull, An Introduction to Composite Materials. Cambridge University Press, Cambridge, 1985.

END

DATE FILMED

11 / 27 / 90